

Supporting Information

Tuning the morphological appearance of iron(III) fumarate: impact on material characteristics and biocompatibility

Patrick Hirschle,¹ Christian Hirschle,² Konstantin Böll,³ Markus Döblinger,¹ Miriam Höhn,⁴ Joshua M. Tuffnell,^{5,6} Christopher W. Ashling,⁵ David A. Keen,⁶ Thomas D. Bennett,⁵ Joachim O. Rädler,⁷ Ernst Wagner,⁴ Michael Peller,³ Ulrich Lächelt,⁴ Stefan Wuttke^{1,8,9} *

¹Department of Chemistry and Center for NanoScience (CeNS), LMU Munich, Butenandtstraße 11 81377 Munich, Germany

²Ruhr-Universität Bochum, Institut für Geologie, Mineralogie und Geophysik, Universitätsstraße 150, 44801 Bochum, Germany

³Department of Radiology, University Hospital, LMU Munich, 81377 Munich, Germany

⁴Department of Pharmacy and Center for NanoScience (CeNS), LMU Munich, Butenandtstraße 5-13 81377 Munich, Germany

⁵Department of Materials Science and Metallurgy, University of Cambridge, 27 Charles Babbage Road, Cambridge CB3 0FS, United Kingdom

⁶ISIS Facility, Rutherford Appleton Laboratory Harwell Campus, Didcot, Oxon, OX11 0QX, UK

⁷Faculty of Physics, Soft Condensed Matter, Ludwig-Maximilians-University, Munich, Germany

⁸School of Chemistry, College of Science, University of Lincoln, Brayford Way, Brayford Pool, Lincoln LN6 7TS, United Kingdom

⁹BCMaterials, Basque Center for Materials, UPV/EHU Science Park, 48940 Leioa, Spain

E-Mail corresponding author: stefan.wuttke@cup.uni-muenchen.de

Table of Contents

1. Methods and Characterization.....	4
1.1 Powder X-ray Diffraction	4
1.2 Transmission Electron Microscopy	4
1.3 Scanning Electron Microscopy	4
1.4 Pair Distribution Function Analysis.....	5
1.5 Nitrogen Sorption.....	5
1.6 Magnet Resonance Imaging.....	5
1.7 <i>In-situ</i> X-ray Diffraction	5
1.8 Inductively Coupled Plasma Optical Emission Spectroscopy	6
1.9 Thermogravimetric Analysis.....	6
1.10 Cell Culture	6
2. Experimental Section	7
2.1 Chemicals.....	7
2.2 Synthesis of the 4 different Iron(III) fumarate Variants	7
Spherical Nanoparticles.....	7
Needle-shaped Microparticles	7
Dipyramidal Nanoparticles.....	7
Dipyramidal Microparticles	8
2.3 Optimization of the aqueous and DMF based Iron(III) fumarate Synthesis.....	8
Microfluidic Synthesis of Iron(III) fumarate in DMF	8
Microfluidic Synthesis of Iron(III) fumarate in Water.....	8
Solvothermal Synthesis of Iron(III) fumarate in DMF	9
Solvothermal Synthesis of Iron(III) fumarate in Water	9
Microwave Synthesis of Iron(III) fumarate in DMF	9

Microwave Synthesis of Iron(III) fumarate in water.....	10
Room Temperature Precipitation of Iron(III) fumarate in DMF.....	10
Room Temperature Precipitation of iron(III) fumarate in Water.....	11
2.4 MTT Assay	11
2.5 CellTiterGlo Assay	11
3. Supplementary Figures and Tables	12
4. Calculations on the Theoretical Particle Surface Area.....	51
5. References	52

1. Methods and Characterization

1.1 Powder X-ray Diffraction

X-ray diffraction experiments were performed on a *STOE Transmissions-Diffraktometer System STADI P* with Ge(111) primary monochromator using $\text{CuK}_{\alpha 1}$ -radiation. The device operates in a transmission setup derived from Debye-Scherrer geometry where the dried sample is fixed between two polymer foils. Analysis was conducted with the included software package *WinXPOW RawDat v3.0.2.5* and *WinXPOW PowDat_n v3.0.2.7*. Lattice parameter refinement was done in UnitCell using 11-19 reflections per sample. Peak positions were corrected based on an internal silicon standard. All diffraction patterns depict an additional low intensity reflection at $24.12 - 24.14^\circ$ that cannot be explained completely by the published structure of MIL-88A. This reflection could be indexed (113), which should not be present in the space group P-62c. It might be caused by an impurity, which formed during the synthesis as the dried samples have proven stable in air over the course of the measurement.

1.2 Transmission Electron Microscopy

TEM samples were prepared by drying an ethanolic dispersion of the X-ray amorphous spherical nanoparticles on a carbon-coated copper grid. Electron microscopy and electron diffraction was performed with a *Titan Themis (FEI)* operated at 300 kV.

1.3 Scanning Electron Microscopy

Sample preparation was performed by drying ethanolic dispersions of the respective samples on a carbon film fixed on an aluminum sample holder under air. After subsequent carbon sputtering the samples were measured using a *Helios G3 UC (FEI)* scanning electron microscope. If not stated otherwise the microscope was operated at 3 kV using a trough-lens detector. To visualize particles below the sample surface the setup was operated at 15 kV using a mirror detector which is also mentioned in the respective pictures.

1.4 Pair Distribution Function Analysis

Data were obtained at the I15-1 beamline, Diamond Light Source, UK ($\lambda = 0.161669 \text{ \AA}$, 72 keV). All samples were vacuum dried for 2 h at room temperature and finely ground before packing into sealed 1.17 mm (inner) diameter borosilicate capillaries. Data were taken of the background, empty capillary, and of all four samples to a Q_{max} of 24 \AA^{-1} . A 50% beam absorber was required for the acquisition of the data for the dipyrnidal nanoparticles and dipyrnidal microparticles samples to prevent oversaturation of the detector. Normalised total scattering data were corrected individually using the GudrunX program^{5,6} to obtain PDFs of each sample (Figure S24). Predicted $G(r)$ patterns of the samples were generated using crystallographic information files available online⁷ and the PDFGUI software⁸.

1.5 Nitrogen Sorption

Nitrogen sorption experiments were performed on dried powders (9-56 mg) of the respective samples. Prior to the measurements the samples were outgassed at $120 \text{ }^\circ\text{C}$ in vacuum for 24 h. All nitrogen sorption experiments were conducted on an *Autosorb-1 (Quantachrome)* using the software *ASiQwin v3.0* for data evaluation. The linearized form of the BET equation was used to calculate BET surface areas. For the calculation of the pore size distribution of the microparticles a QSDFT adsorption based model was used assuming cylindrical pores. Due to the mesotexturing of the spherical nanoparticle sample the pore size distribution of these particles was calculated with a QSDFT adsorption based model assuming cylindrical and slit pores.

1.6 Magnet Resonance Imaging

MRI experiments were performed either on dispersions of larger iron(III) fumarate variants while they were embedded in 0.2 wt% Xanthan Gel (2 mL) or of the spherical nanoparticles when suspended in water (2 mL). The Xanthan gels were prepared by generating aqueous dispersion of the respective particle concentrations and subsequent addition of dry Xanthan. After vortexing the particle dispersion were sonicated for 20 min followed by additional pipetting and repeated sonication for 30 min.

1.7 In-situ X-ray Diffraction

In-situ X-ray diffraction experiments were performed on dispersions the samples with sharp reflections in Figure 3. The experiments were performed on a *STOE Transmissions-Diffraktometer System STADI P* with Ge(111) primary monochromator using $\text{CuK}_{\alpha 1}$ -radiation operating in

transmission geometry. The particle dispersions were placed in sealed glass capillary tubes. Analysis was conducted with the included software package *WinXPOW RawDat v3.0.2.5*, *WinXPOW PowDat_n v3.0.2.7* and *WinXPOW Index v3.0.2.1*. For refinement of the lattice parameters 5-11 reflections were considered. Additionally the X-ray diffraction pattern of an empty glass capillary was recorded (Figure S35). The capillary corresponds to a reflection at the angle of 8.495 ° which can be visible in a few of the *in-situ* diffraction patterns.

1.8 Inductively Coupled Plasma Optical Emission Spectroscopy

ICP-OES measurements were performed in on dried samples that were digested using 10% HNO₃ (*Aristar VWR*). The setup consisted of an *ICP AES Vista RL* with a *CCD simultaneous ICP AES* detector (*Agilent*). Measurements were performed with Argon plasma at 1.2 kW in 3 x 8 s periods with 45 s stabilization time. Wavelengths used were at 238 nm and 259 nm.

1.9 Thermogravimetric Analysis

For gravimetric measurements all dried samples of the respective iron(III) fumarate variants (Figure S25) were measured on a *TASC 414/4 (Netzsch)* under synthetic air at a flow rate of 25 mL/min. The experiments were performed with a heating rate of 10 °C/min up to 900 °C. The resulting data was evaluated using the software *Proteus v4.3*.

1.10 Cell Culture

HeLa cells (ATCC CCL-2) were grown in RPMI-1640 medium (L-alanyl-glutamine and sodium bicarbonate) supplemented with 10 % FBS, 100 U/mL penicillin, 100 µg/mL streptomycin. The cells were cultured in ventilated flasks in the cell incubator at 37 °C and 5 % CO₂ in a humidified atmosphere. Cells were passaged at approx. 80 % confluency.

2. Experimental Section

2.1 Chemicals

Ethanol (VWR, 99.9%), Iron(III) chloride hexahydrate (*Grüssing*, 99%), Fumaric acid (*Sigma*, $\geq 99.0\%$), *N,N* Dimethylformamide (DMF, *VWR*, 99.9%), Xanthan gum from *Xanthoma campestris* (*Sigma*).

2.2 Synthesis of the 4 different Iron(III) fumarate Variants

In this section the synthesis protocols used to generate the four iron(III) fumarate variants that were later characterized for functionality and biocompatibility are shown.

Spherical Nanoparticles

A solution of $\text{FeCl}_3 \cdot 6 \text{H}_2\text{O}$ (2168 mg, 8.02 mmol) in water (40 mL, *Merck, Milli-Q*) was prepared. Fumaric acid (970 mg, 8.36 mmol) was added under stirring. After incubation at room temperature (2 min) the reaction was stopped and washed three times by centrifuging (7197 rcf, 20 min) and redispersing in ethanol.

Needle-shaped Microparticles

A reaction mixture of fumaric acid (485 mg, 4.18 mmol) and $\text{FeCl}_3 \cdot 6 \text{H}_2\text{O}$ (1084 mg, 4.01 mmol) in water (20 mL, *Merck, Milli-Q*) was prepared. The reaction mixture was placed in a 50 mL Schott glass vial and put into an oven for 24 h at 80 °C. The resulting particles were washed three times by centrifuging (7197 rcf, 20 min) and redispersing in ethanol.

Dipyramidal Nanoparticles

Fumaric acid (485 mg, 4.18 mmol) and $\text{FeCl}_3 \cdot 6 \text{H}_2\text{O}$ (1084 mg, 4.01 mmol) were dissolved in DMF (20 mL). This reaction mixture was placed in a 80 mL Teflon tubes and put in a microwave reactor (*Synthos 3000, Anton Paar*) along with a reference solution containing $\text{FeCl}_3 \cdot 6 \text{H}_2\text{O}$ (1084 mg, 4.01 mmol) in DMF (20 mL) and two additional vessels containing tap water (20 mL). A reaction program consisting of first heating the sample for 30 s up to 120 °C and subsequent holding of this temperature for 5 min was used. At the end of this program the reaction was quenched by pouring the hot reaction mixture in DMF (room temperature, 50 mL). The resulting product was washed with DMF (40 mL) washed three times by centrifuging (7197 rcf, 20 min) and redispersing in DMF.

Dipyramidal Microparticles

A stock solution of fumaric acid (194 mg, 1.67 mmol) and $\text{FeCl}_3 \cdot 6 \text{H}_2\text{O}$ (433 mg, 1.604 mmol) in DMF (8 mL) was prepared and divided equally into 8 1.5 mL Eppendorf tubes. The reaction mixtures were placed in an oven for 30 min at 120 °C. The resulting particles were washed three times by centrifuging (16873 rcf, 10 min) and redispersing in DMF.

2.3 Optimization of the aqueous and DMF based Iron(III) fumarate Synthesis

In this section reaction parameters for the morphological optimization of iron(III) fumarate in water and DMF are shown.

Microfluidic Synthesis of Iron(III) fumarate in DMF

This microfluidic approach was based on a continuous flow reactor (Figure S5) heating a premixed a solution of fumaric acid (485 mg, 4.18 mmol) and $\text{FeCl}_3 \cdot 6 \text{H}_2\text{O}$ (1084 mg, 4.01 mmol) in DMF (20 mL). Using a syringe pump, the solution was then pressed through a microfluidic channel consisting of a Teflon tube (120 cm, 1/16" outer diameter). The larger segment of this tubing (1 m) tubing was immersed in an oil bath (120 °C) in order to heat the traversing reaction solution. By varying the speed of the syringe pumps, different incubation times (1 min, 2min, 4 min, 5 min, 8 min, 16 min, and 30 min) for the particle synthesis were preset. The respective fractions (Figure S6) were collected in an Eppendorf Tube and washed three times by centrifuging (16873 rcf, 10 min) and redispersing in DMF.

Microfluidic Synthesis of Iron(III) fumarate in Water

This microfluidic setup was based on the continuous flow reactor shown in Figure S5 left. Using two syringe pumps precursor aqueous (*Merck, Milli-Q*) solutions of fumaric acid (40 mg, 0.34 mmol, 20 mL) and $\text{FeCl}_3 \cdot 6 \text{H}_2\text{O}$ (90 mg, 0.33 mmol, 20 mL) were then pressed through a microfluidic channel consisting of a Teflon tube (15 cm, 1/16" Outer diameter) into a T-junction (*Elveflow*) serving as a mixing zone. Following this junction the reaction mixture traversed a heating zone (1 m) in which the Teflon tube was immersed in a water bath (80 °C). By varying the speed of the syringe pumps, different incubation times (1 min, 2 min, 3 min, and 10 min) for the particles were preset. The respective fractions (Figure S14) were collected in an Eppendorf Tube and washed three times by centrifuging (16873 rcf, 10 min) and redispersing in ethanol.

Solvothermal Synthesis of Iron(III) fumarate in DMF

A stock solution of fumaric acid (485 mg, 4.18 mmol) and $\text{FeCl}_3 \cdot 6 \text{H}_2\text{O}$ (1084 mg, 4.01 mmol) in DMF (20 mL) was prepared. For low concentration experiments this stock solution was further diluted with DMF in a 1:10 ratio. To test the temperature necessary for iron(III) fumarate formation under these conditions small fractions of the concentrated stock solution (1.0 mL) were put into 1.5 mL Eppendorf tubes and incubated in an Thermoshaker (*TS-100, PeqLab*) at RT, 30 °C, 40 °C, 50 °C and 60 °C and heated for 18 h under monitoring. Due to slower particle formation in case of the lower concentrated solution this process was repeated at 70 °C, 80 °C, 100 °C and 120 °C in an oven. In these experiments precipitation of iron(III) fumarate could only be observed for heating at temperatures above 100 °C (Figure S4). Additional optimization was done at 120 °C using the concentrated iron(III) fumarate stock solution in DMF in volumes of 1 mL. At specific times (1 min, 2 min, 5 min, 10 min, 20 min, 30 min, 60 min, 6 h and 24 h) aliquots were removed. Formation of iron(III) fumarate could be observed from 30 min onwards. In case of product formation (Figure S2) the solution was washed three times by centrifuging and redispersing in DMF.

Solvothermal Synthesis of Iron(III) fumarate in Water

A reaction mixture of fumaric acid (485 mg, 4.18 mmol) and $\text{FeCl}_3 \cdot 6 \text{H}_2\text{O}$ (1084 mg, 4.01 mmol) in water (20 mL, *Merck, Milli-Q*) was produced. Aliquots of the dispersion (1.0 mL) were put into 1.5 mL Eppendorf tubes and incubated at 80 °C in a thermoshaker (*TS-100, PeqLab*). At specific times (1 min, 5 min, 20 min, 24 h and 7 d) these samples were removed from the thermoshaker. The samples (Figure S13) were washed three times by centrifuging and redispersing in ethanol.

Lower concentration experiments were performed by dissolving fumaric acid (16 mg, 138 μmol) and $\text{FeCl}_3 \cdot 6 \text{H}_2\text{O}$ (36.6 mg, 136 μmol) each in water (10 mL, *Merck, Milli-Q*). These solutions were mixed and the resulting reaction mixture heated in 1.5 mL Eppendorf tubes (80 °C, 1.0 mL reaction volume) using a thermoshaker (*TS-100, PeqLab*). At specific times (5 min and 20 min) heating was stopped and the samples (Figure S15) were washed three times by centrifuging (16873 rpm, 10 min) and redispersing in ethanol.

Microwave Synthesis of Iron(III) fumarate in DMF

Fumaric acid (485 mg, 4.18 mmol) and $\text{FeCl}_3 \cdot 6 \text{H}_2\text{O}$ (1084 mg, 4.01 mmol) were dissolved in DMF (20 mL) under stirring. The clear yellow solution was placed in 80 mL Teflon tubes and put in a microwave reactor (*Synthos 3000, Anton Paar*) along with a reference solution containing

FeCl₃ · 6 H₂O (1084 mg, 4.01 mmol) in DMF (20 mL) and two additional vessels containing tap water (20 mL). The microwave programs shown in Table S1 were applied. After finishing the program, the crystal growth was stopped by pouring the hot reaction solution into DMF (RT, 50 mL). The product (Figure S7) was washed three times by centrifuging (7197 rcf, 20 min) and redispersing in DMF.

Table S1. Microwave parameters of the synthesis of iron(III) fumarate in DMF.

Heating to 120 °C	Incubation at 120 °C
30 s	2 min
30 s	3 min
30 s	5 min

Microwave Synthesis of Iron(III) fumarate in water

Fumaric acid (485 mg, 4.18 mmol) and FeCl₃ · 6 H₂O (1084 mg, 4.01 mmol) were dissolved in Millipore water (20 mL, *Merck, Milli-Q*). The orange dispersion was placed in a Teflon tube (80 mL) and put in a microwave reactor (*Synthos 3000, Anton Paar*) along with a reference solution containing FeCl₃ · 6 H₂O (1084 mg, 4.01 mmol) in water (20 mL, *Merck, Milli-Q*) and two additional vessels containing tap water (20 mL). The microwave programs shown in Table S2 were applied. After finishing the program, reaction was quenched by pouring the hot reaction solution into water (RT, 50 mL). The product (Figure S12) was washed three times by centrifuging (7197 rcf, 20 min) and redispersing in ethanol.

Table S2. Microwave parameters of the synthesis of iron(III) fumarate in water.

Heating to 80 °C	Incubation at 80 °C
30 s	1 min
30 s	2 min
30 s	5 min

Room Temperature Precipitation of Iron(III) fumarate in DMF

A solution of fumaric acid (485 mg, 4.18 mmol) and FeCl₃ · 6 H₂O (1084 mg, 4.01 mmol) in DMF (20 mL) was incubated at room temperature for three weeks. No particle formation could be monitored.

Room Temperature Precipitation of iron(III) fumarate in Water

A reaction mixture of fumaric acid (485 mg, 4.18 mmol) and $\text{FeCl}_3 \cdot 6 \text{H}_2\text{O}$ (1084 mg, 4.01 mmol) in water (20 mL, *Merck, Milli-Q*) was incubated at room temperature. Aliquots were taken after a certain reaction time (2 min, 2 h, 8 h, 24 h, 4 d and 7 d). The samples (Figure S10) were washed three times by centrifuging (16873 rcf, 10 min) and redispersing in ethanol.

A lower concentration experiment was performed by dissolving fumaric acid (16 mg, 138 μmol) and $\text{FeCl}_3 \cdot 6 \text{H}_2\text{O}$ (36.66 mg, 136 μmol) each in 10 mL water (*Merck, Milli-Q*). The solutions were unified and the resulting reaction mixture incubated for 7 d at room temperature. The final product (Figure S16) was washed three times by centrifuging (7197 rcf, 20 min) and redispersing in ethanol

2.4 MTT Assay

One day prior to the experiment HeLa cells were seeded at a density of 5.000 cells per well in 96-well plates (TPP Techno Plastic Products AG). 24 h after cell seeding, the medium was replaced by 80 μL fresh medium. The different iron(III) fumarate particle suspensions were diluted in water to 100, 200, 500 and 1000 $\mu\text{g/mL}$ and 20 μL of the dilutions was added per well (dilution factor 1:5). The cells were incubated for 24, 48 or 72 hours at 37 °C and 5% CO_2 . 10 μL MTT (3-(4,5-dimethylthiazol-2-yl)-2,5-diphenyltetrazolium bromide) (5 mg/mL) resulting in a final concentration of 0.5 mg/mL was added to each well. The plates were incubated for 1 h at 37 °C. Unreacted dye and medium were removed and the 96-well plates frozen at -80 °C for 60 min. After thawing, 100 μL DMSO was added to each well and the plates were incubated for 30 minutes at 37 °C under shaking to dissolve the purple formazan product. Absorbance [A] was quantified at 590 nm with a background correction at 630 nm using a microplate reader (TecanSpectrafluor Plus, Tecan, Switzerland). All treatments were performed in quintuplicates. The relative cell viability (%) normalized to control cells treated with 20% water only was calculated as $([A]_{\text{test}}/[A]_{\text{control}}) \times 100\%$. Mean values +/- standard deviation are reported.

2.5 CellTiterGlo Assay

Cells were seeded and treated for 24, 48 and 72 hours the same way as described in the MTT assay section. After the indicated incubation times, the CellTiter-Glo® assay (Promega GmbH, Walldorf, Germany) was carried out as recommended by the provider. Briefly, the medium was removed and replaced by 50 μL fresh medium per well. The plates were equilibrated to room

temperature during 30 min. Afterwards, 50 μL of the assay reagent solution was added per well and the plates were incubated for 10 min. at room temperature under shaking. The cell lysates (90 μL per well) were transferred into white 96-well plates and the bioluminescence [BL] was measured using a Centro LB 960 plate reader luminometer (Berthold Technologies, Germany). The relative cell viability (%) normalized to control cells treated with 20% water only was calculated as $([\text{BL}]_{\text{test}}/[\text{BL}]_{\text{control}}) \times 100\%$. Mean values \pm standard deviation are reported.

3. Supplementary Figures and Tables

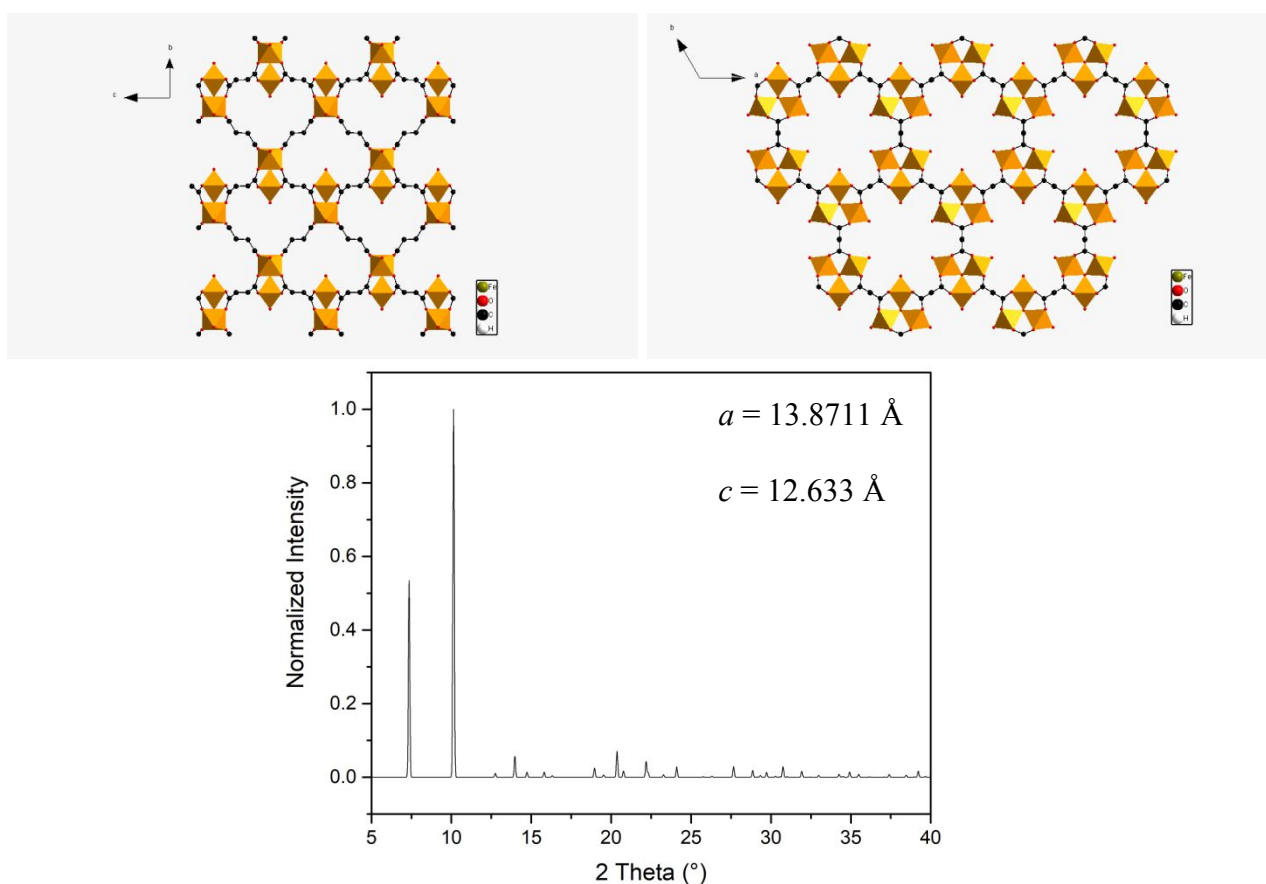


Figure S1. Depiction of the crystal structure of open-pore MIL-88A simulated (Software: *Diamond v3.0, Crystal Impact*) according to data published by Serre.¹ Top left: Depiction of the crystal structure along the *a*-axis. Top right: Depiction of the crystal structure along the *c*-axis. Bottom: Simulated diffraction pattern of open-pore MIL-88(A) along with lattice parameters.

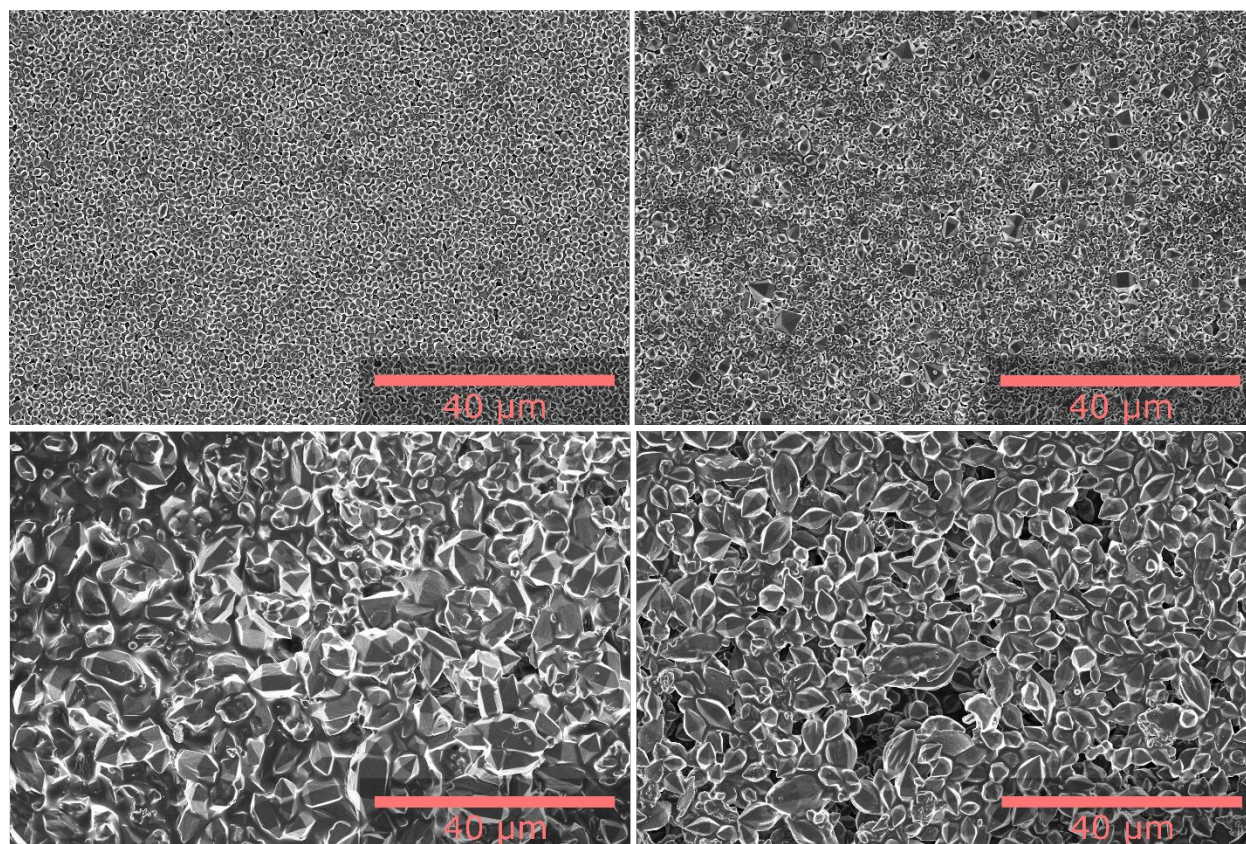


Figure S2. SEM micrographs of iron(III) fumarate microparticles grown solvothermally at 120 °C in DMF for reaction times of 30 min, 60 min, 6 h and 24 h.

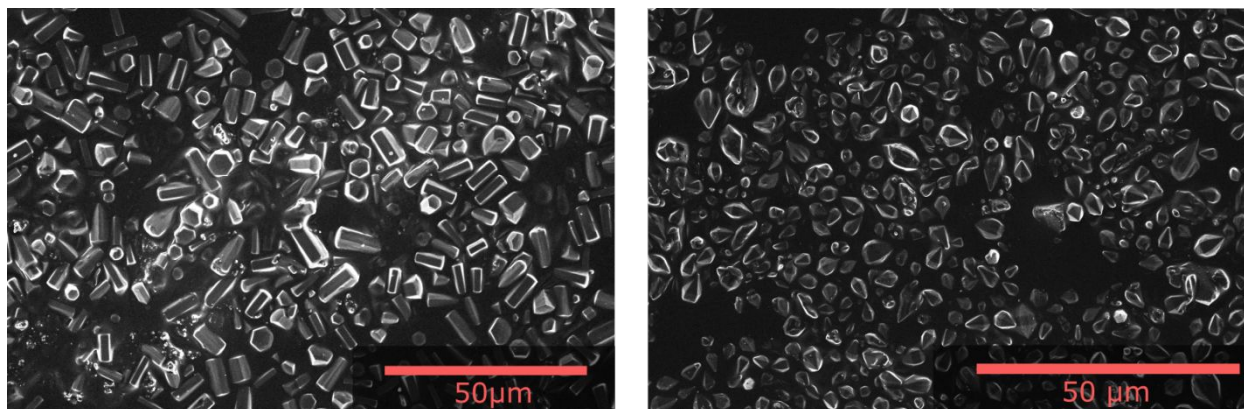


Figure S3. SEM micrographs of iron(III) fumarate microparticles grown solvothermally 120 °C in DMF with 24 h incubation time. Right: Growth from high-concentration stock solution, Left: Growth from low-concentration stock solution.

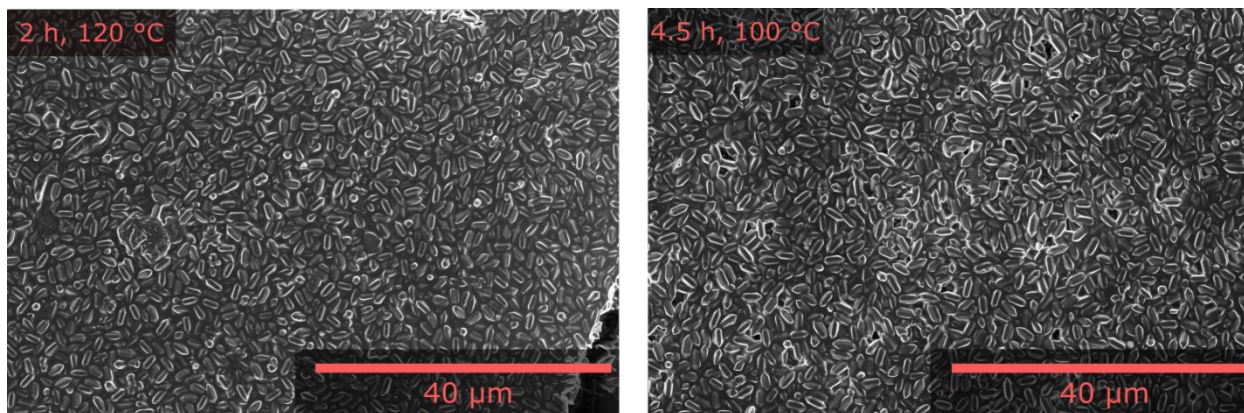


Figure S4. SEM micrographs of iron(III) fumarate microparticles grown solvothermally from a low concentration stock solution at 100 °C and 120 °C in DMF in dependency of reaction time.

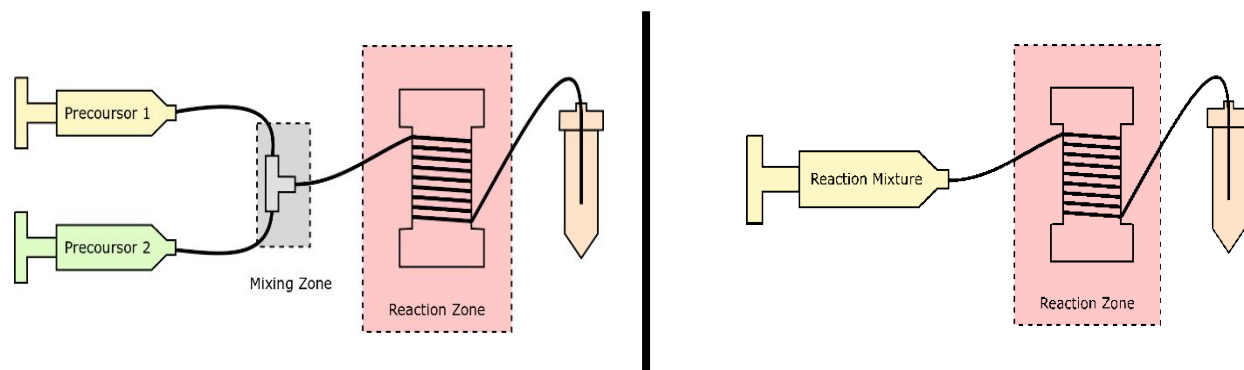


Figure S5. Left: Schematic of the microfluidic setup used for optimization of iron(III) fumarate particles in water: Aqueous precursor solutions of iron(III) chloride (Precursor 1) and fumaric acid (Precursor 2) were pressed into a microfluidic tubing (PTFE, Elveflow, OD 1/16", ID 1/32", length 1.2 m) and mixed in a T-junction. Part of the tubing then traversed a heating zone (water bath, 1 m, 80 °C) before being collected in an Eppendorf tube. **Right:** Schematic illustration of the microfluidic setup used for iron(III) fumarate synthesis in DMF. A premixed reaction mixture containing fumaric acid and iron(III) chloride was pressed into a microfluidic tubing (PTFE, Elveflow, OD 1/16", ID 1/32", length 1.2 m) via a syringe pump. Part of this tubing (1 m) was traversing a heating zone (oil bath, 120 °C) before being collected in an Eppendorf tube.

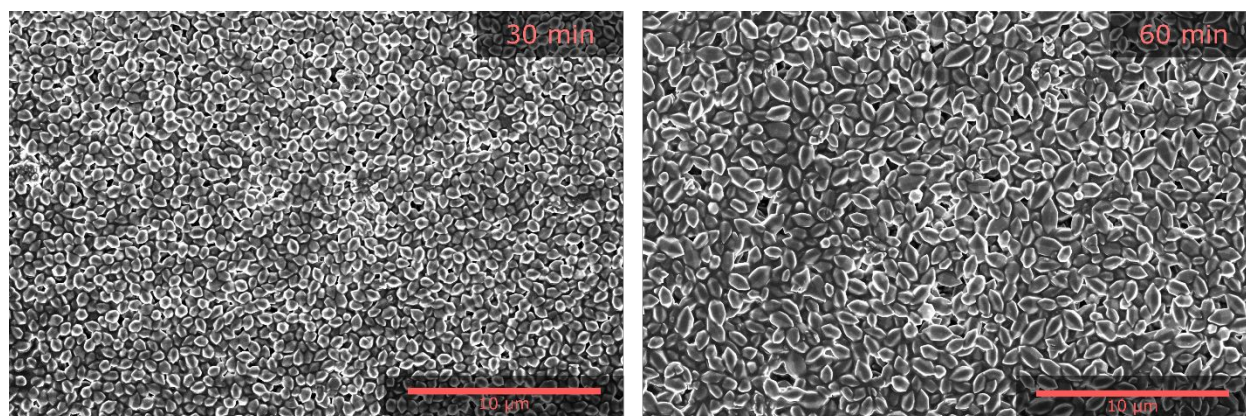


Figure S6. SEM micrographs of iron(III) fumarate microparticles grown in a microfluidic reactor at 120 °C in DMF for reaction times of 30 min and 60 min.

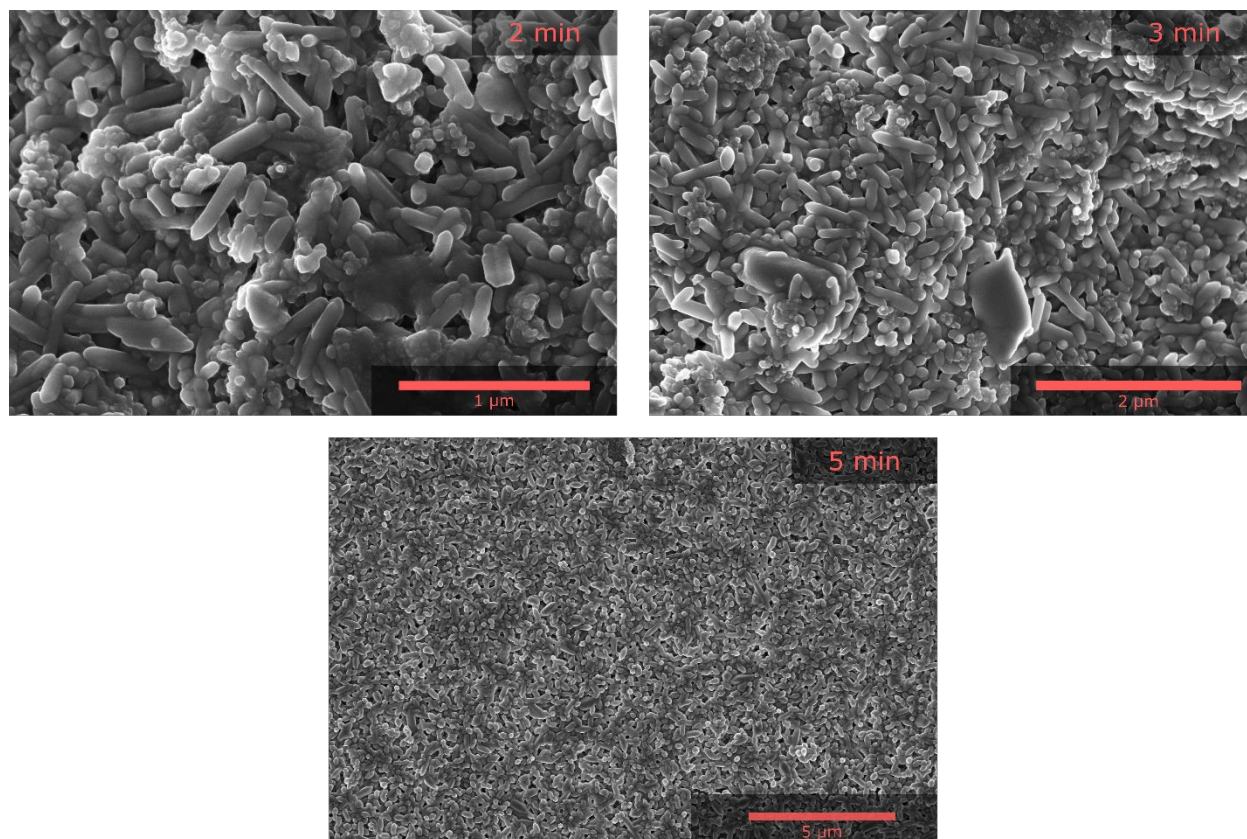


Figure S7. SEM micrographs giving the morphology of iron(III) fumarate nanoparticles grown in a microwave reactor at 120 °C in DMF in dependency of reaction time.

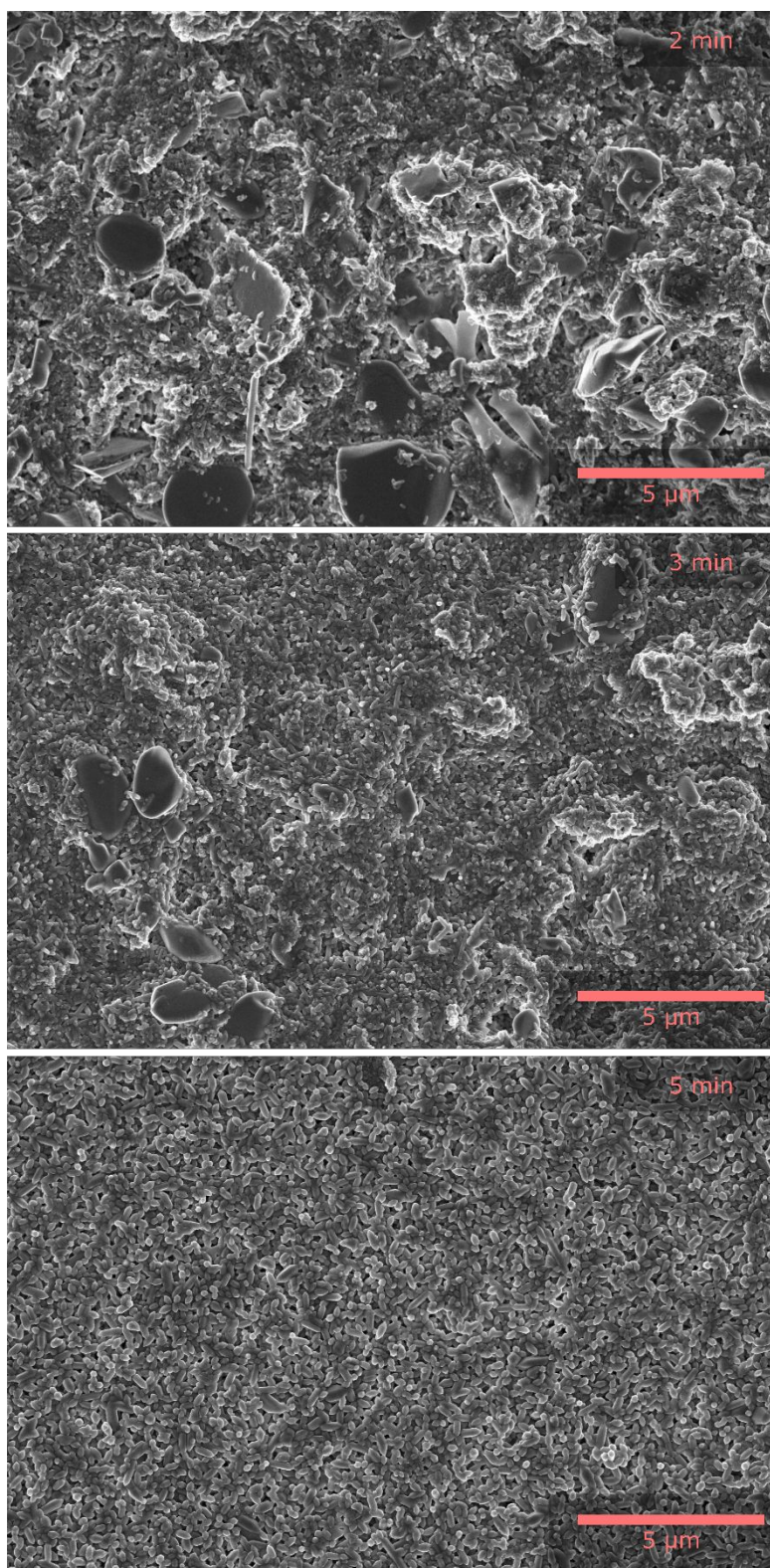


Figure S8. SEM micrographs giving an overview of iron(III) fumarate samples grown in a microwave reactor at 120 °C in DMF in dependency of reaction time.

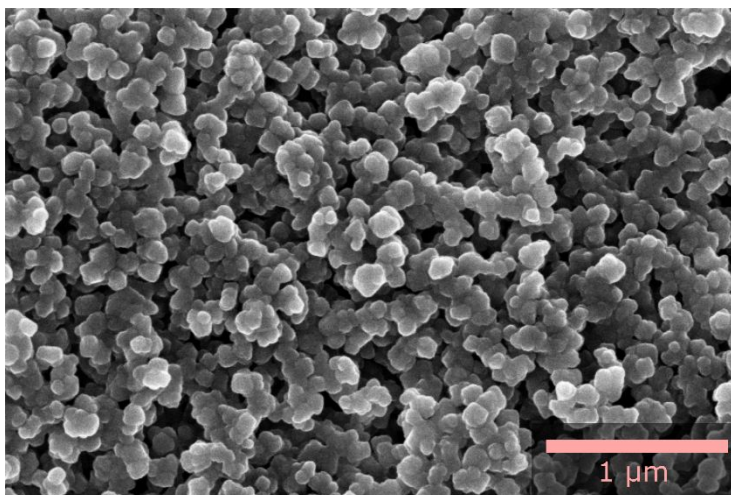


Figure S9. SEM micrograph of spherical iron(III) fumarate particles precipitated immediately after mixing iron(III) chloride and fumaric acid.

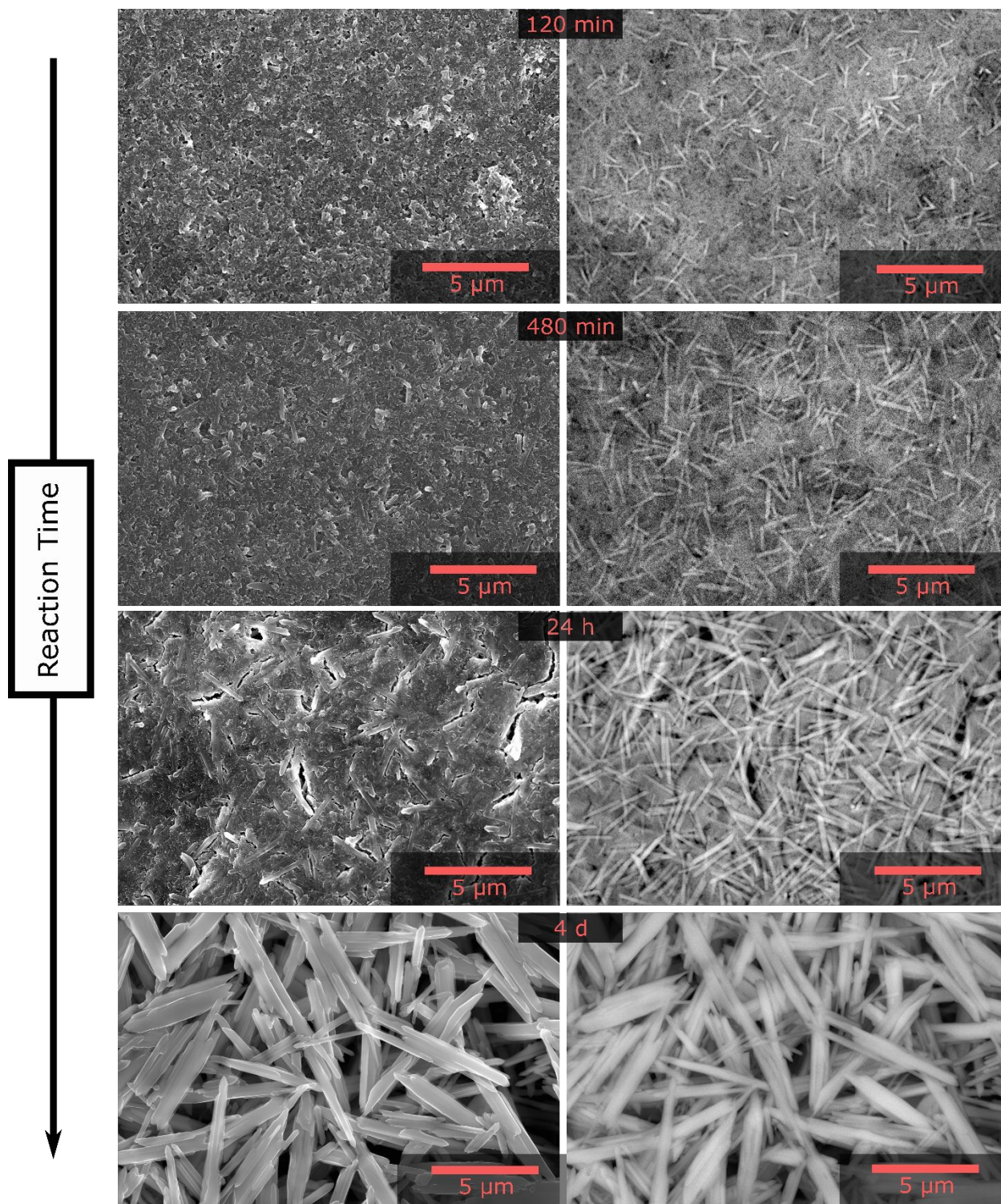


Figure S10. SEM micrographs of iron(III) fumarate nano and microparticles grown at RT in water for reaction times of 2 h, 8 h, 24 h and 4 d. On the left and right side the same spot in each sample is depicted. The micrographs on the right side were recorded at 15 kV using a mirror detector, the micrographs on the left side were recorded at 3 kV using a secondary electron detector.

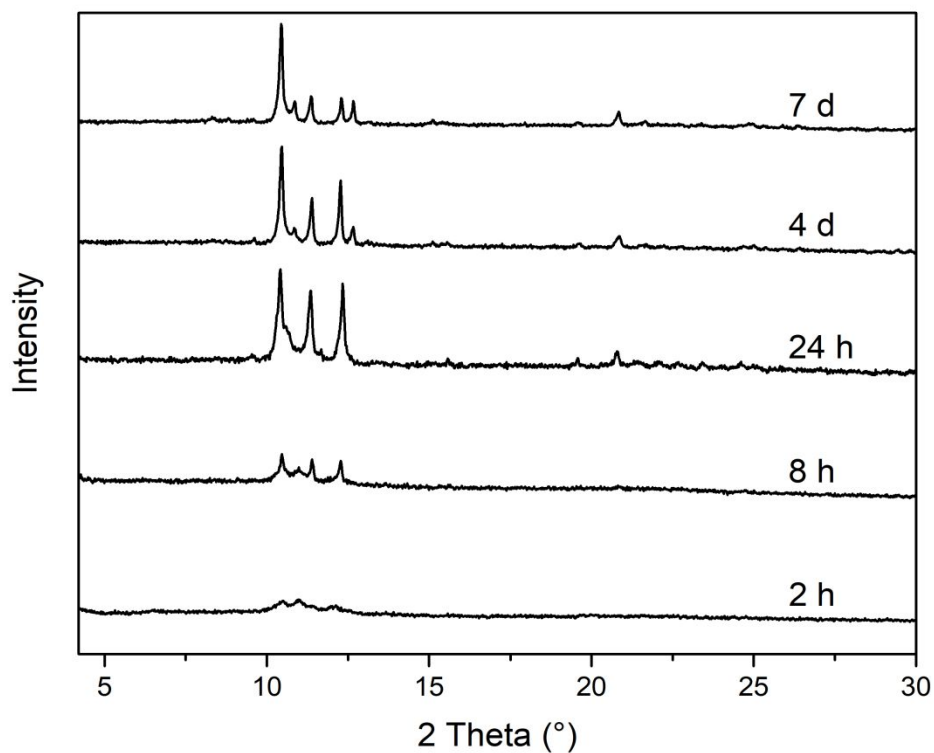


Figure S11. X-ray diffraction patterns of dried aqueous iron(III) fumarate reaction mixtures that were incubated at RT with different reaction times. The reaction was stopped by centrifuging and redispersion in ethanol. With time, the samples become increasingly crystalline. As reported in literature, these reflections during the aqueous synthesis of the MOF do not fully correspond to the final crystal structure of MIL-88A but have similarly been reported elsewhere.^{3,4,4}

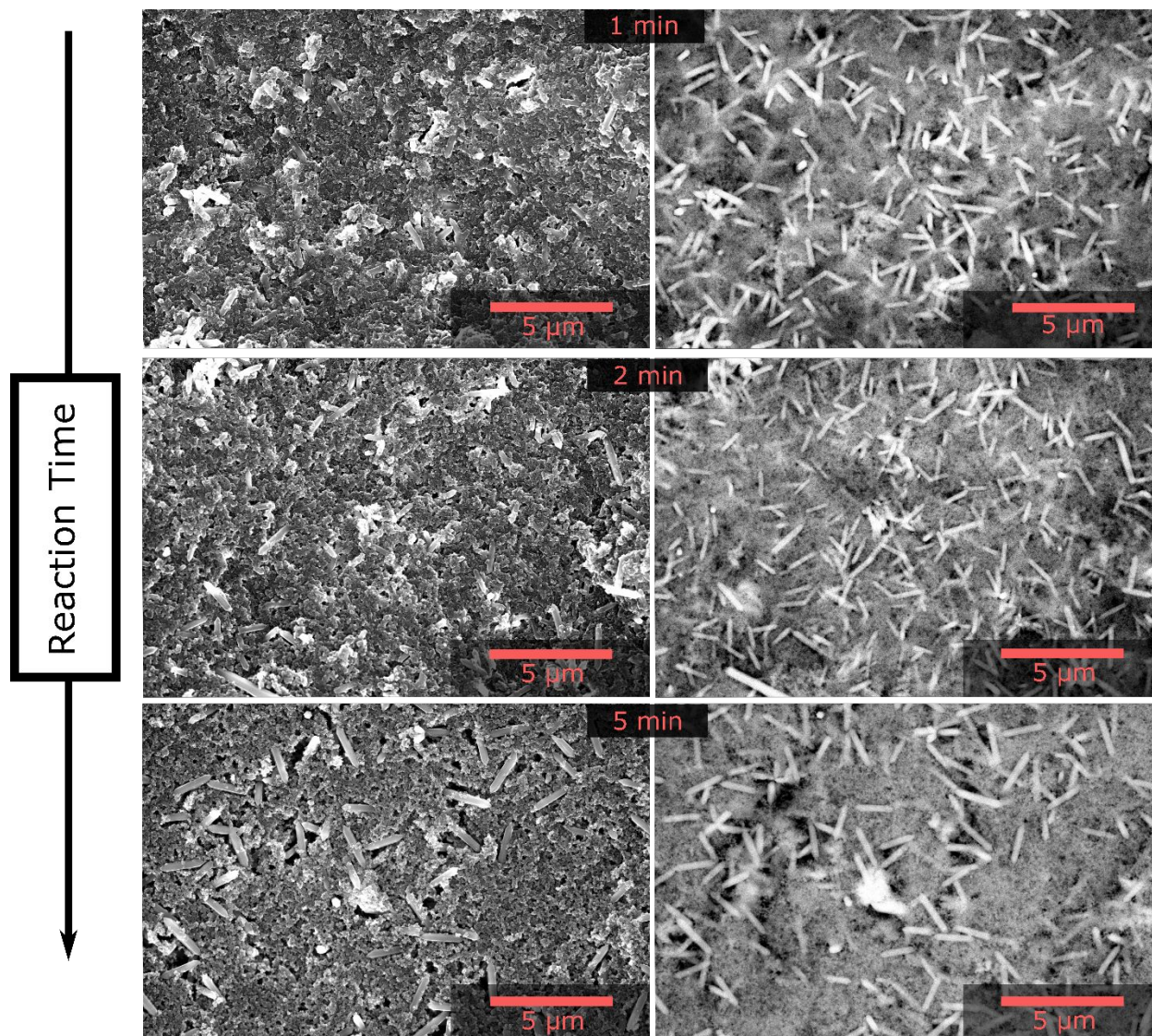


Figure S12. SEM micrographs of iron(III) fumarate nano and microparticles grown in a microwave reactor at 80 °C in water for reaction times of 1 min, 2 min, and 5 min. On the left and right side the same spot in each sample is depicted. The micrographs on the right side were recorded at 15 kV using a mirror detector, the micrographs on the left side were recorded at 3 kV using a secondary electron detector.

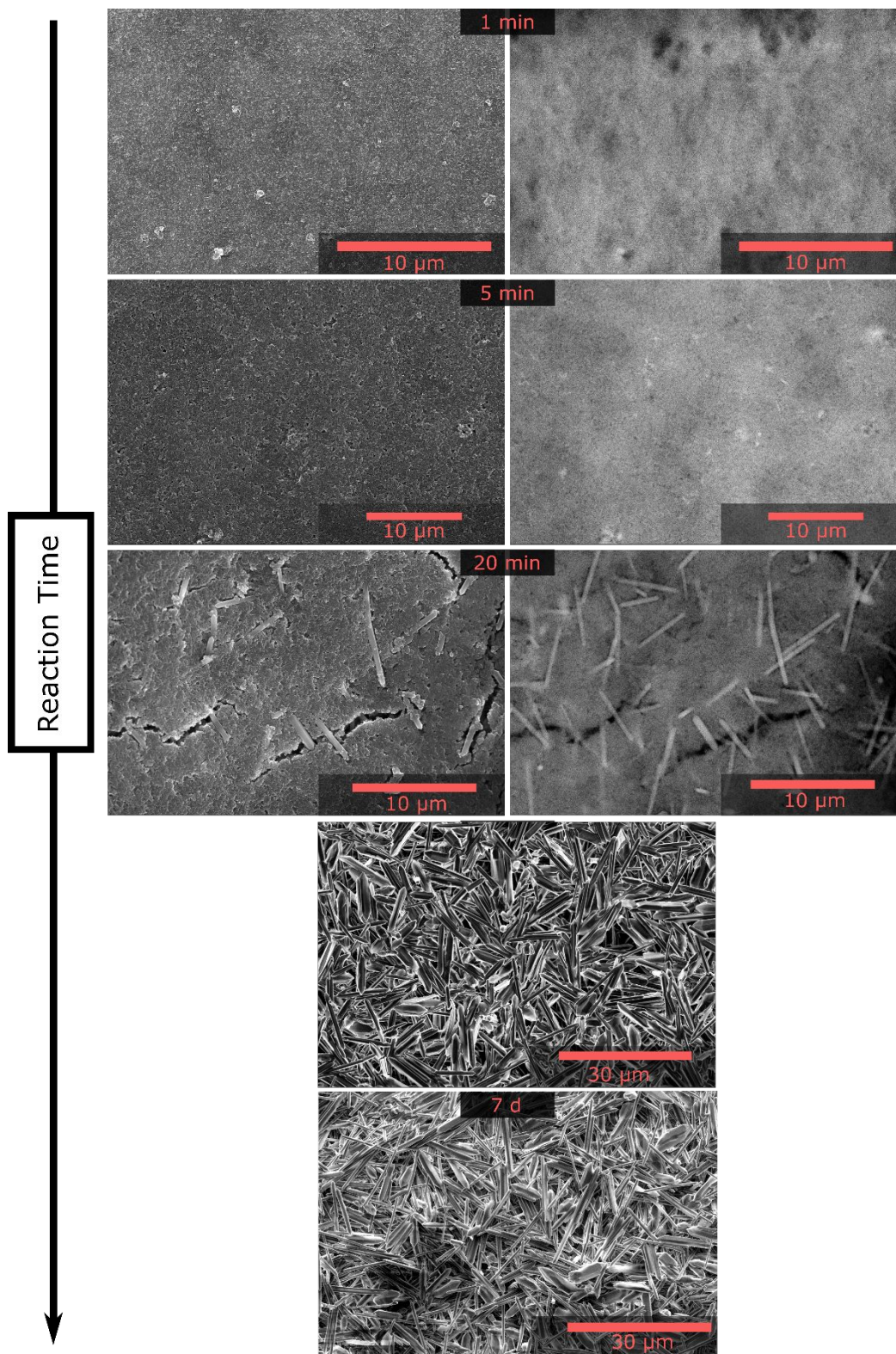


Figure S13. SEM micrographs of iron(III) fumarate nano and microparticles grown solvothermally at 80 °C in water for reaction times of 1 min, 5 min, 20 min, 24 h and 7 d). On the left and right side the same spot in each sample is depicted. The micrographs on the right side were recorded at 15 kV using a mirror detector, the micrographs on the left side were recorded at 3 kV using a secondary electron detector.

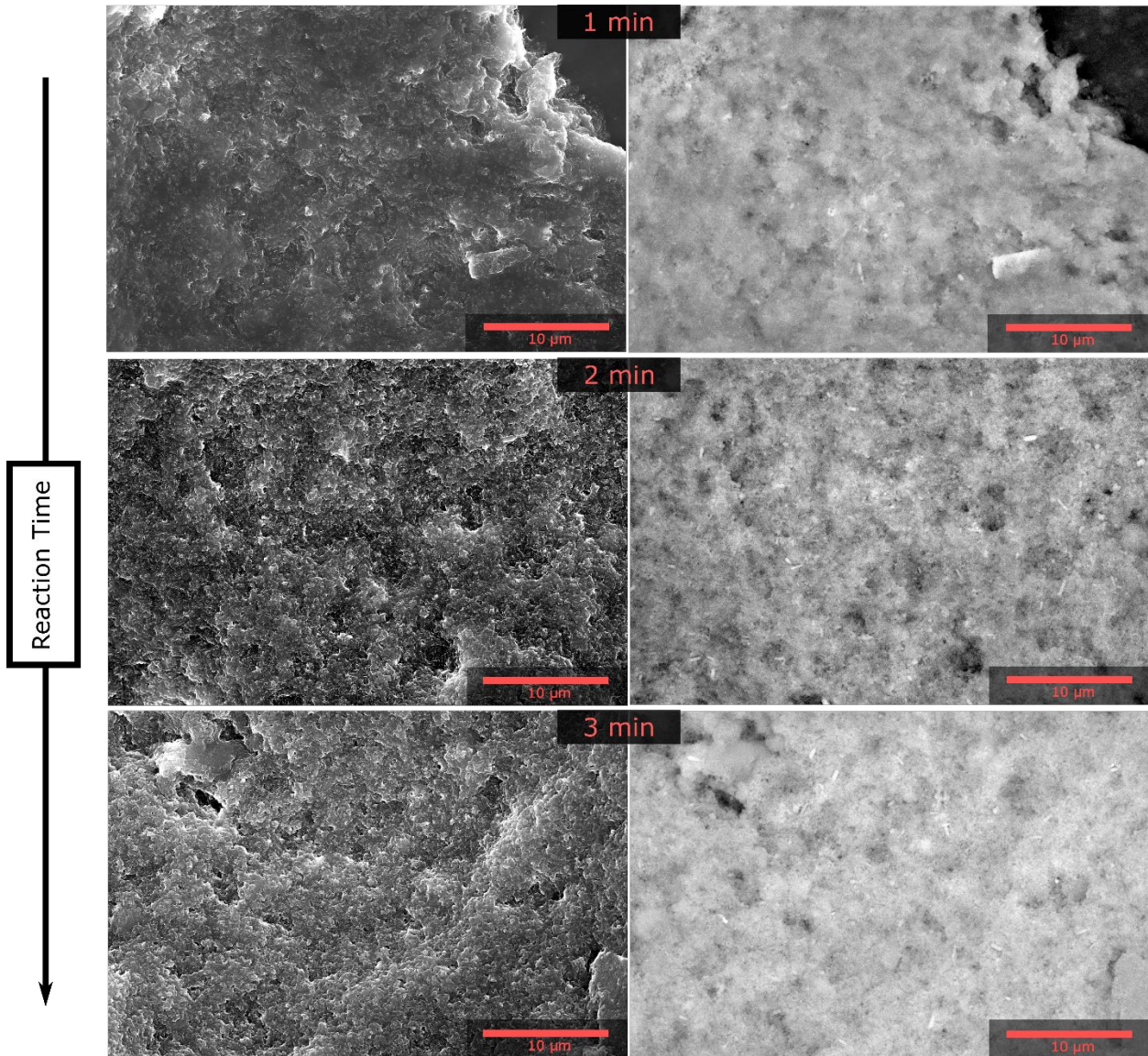


Figure S14. SEM micrographs of iron(III) fumarate nano and microparticles grown in a microfluidic reactor at 80 °C in water for low reaction times (1-3 min). On the left and right side the same spot in each sample is depicted. The micrographs on the right side were recorded at 15 kV using a mirror detector, the micrographs on the left side were recorded at 3 kV using a secondary electron detector.

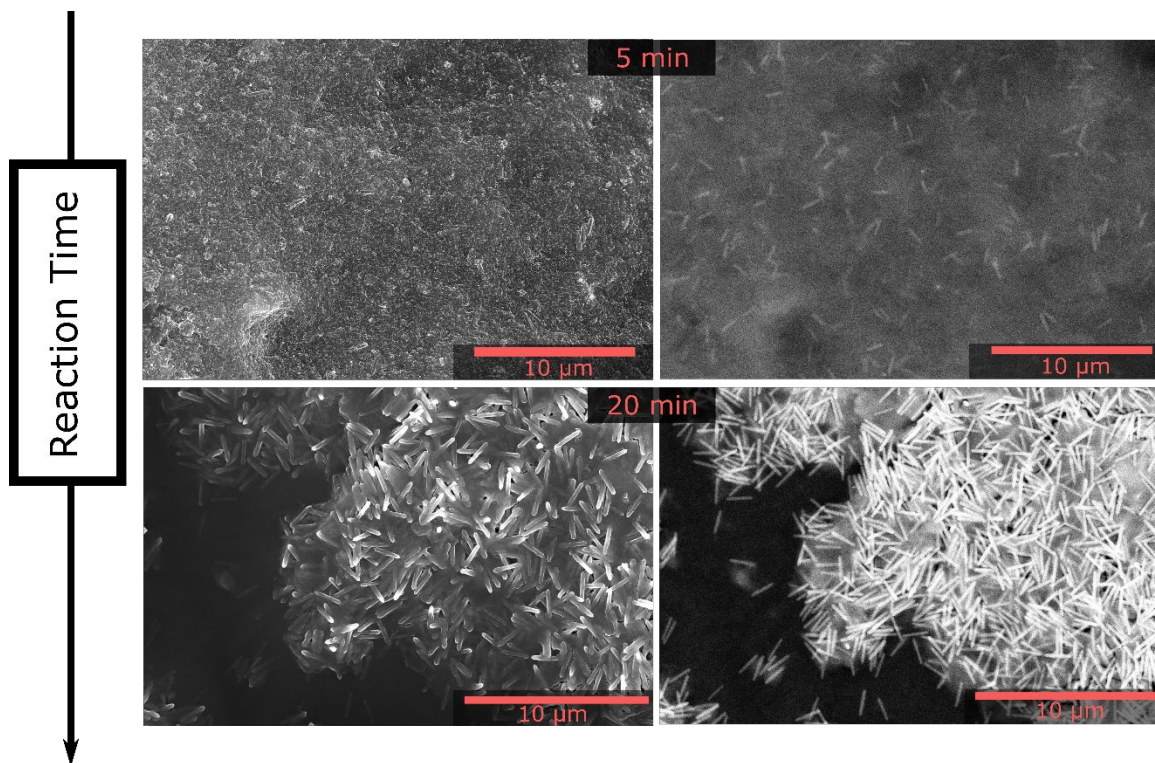


Figure S15. SEM micrographs of iron(III) fumarate nano and microparticles grown solvothermally at 80 °C in water at low concentration for reaction times of 5 min and 20 min. On the left and right side the same spot in each sample is depicted. The micrographs on the right side were recorded at 15 kV using a mirror detector, the micrographs on the left side were recorded at 3 kV using a secondary electron detector.

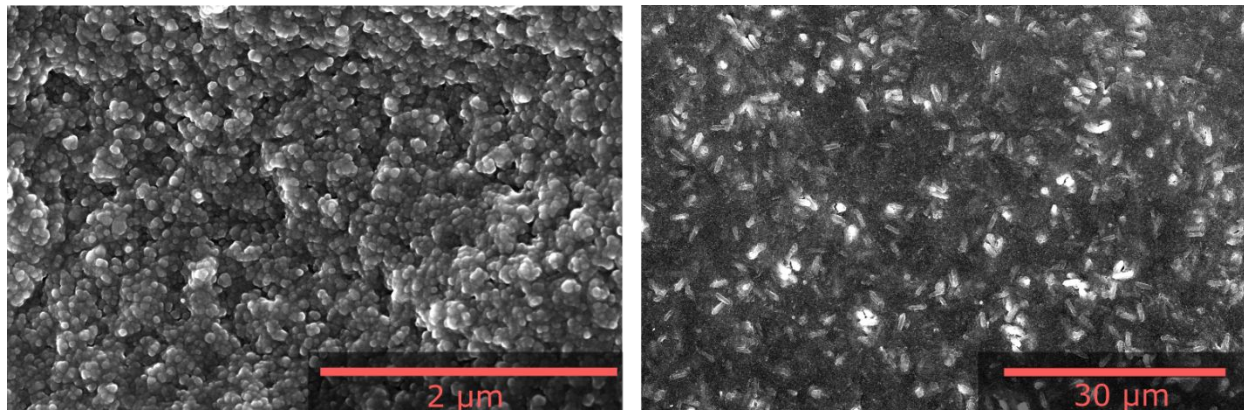


Figure S16. SEM micrographs of iron(III) fumarate nano and microparticles grown at RT in water for 7 d at low concentration. The micrographs on the right side were recorded at 15 kV using a mirror detector, the micrographs on the left side were recorded at 3 kV using a secondary electron detector.

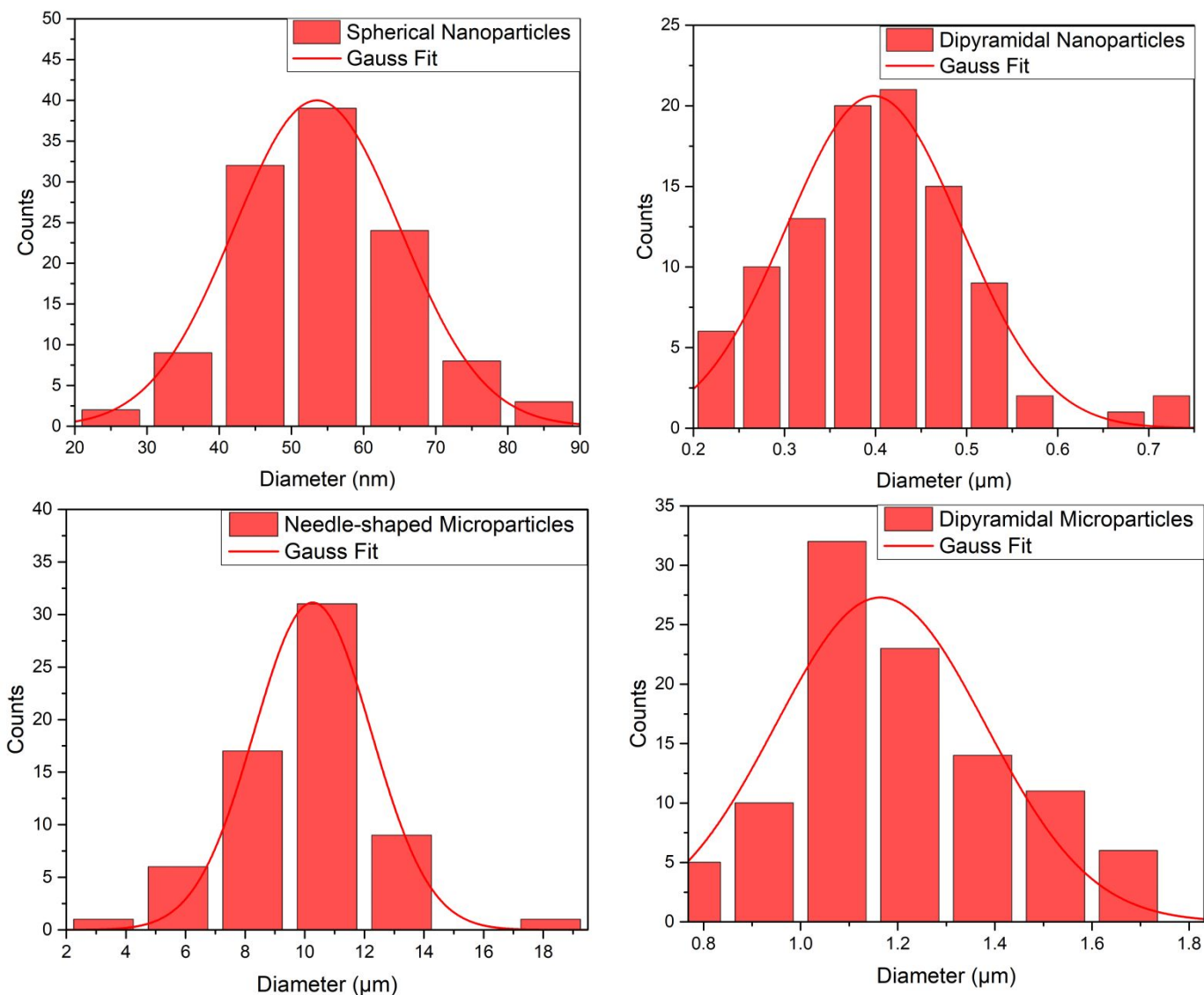


Figure S17. Particle size distributions of the four iron(III) fumarate variants determined from SEM micrographs in Figure 2. Depending on the iron(III) fumarate variant 60-120 particles were measured by hand with the software Imagej v1.52e. Using the software Origin Pro v9.1.0. This data was then plotted in histograms and fitted with a Gaussian fit.

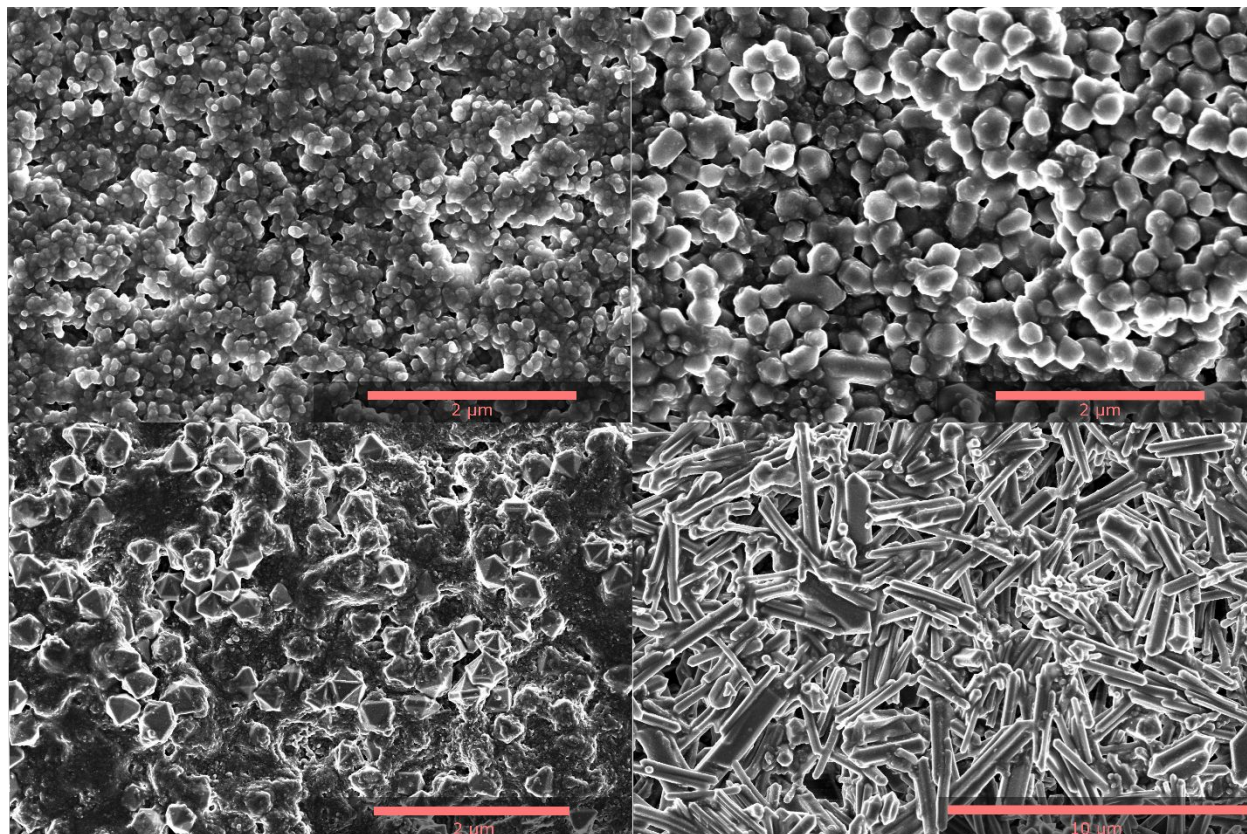


Figure S18. SEM micrographs of iron (III) fumarate particles after 24 h in 20% cell medium. **Top left:** spherical nanoparticles, **top right:** dipyramidal nanoparticles, **bottom left:** dipyramidal microparticles, **bottom right:** needle-shaped microparticles.

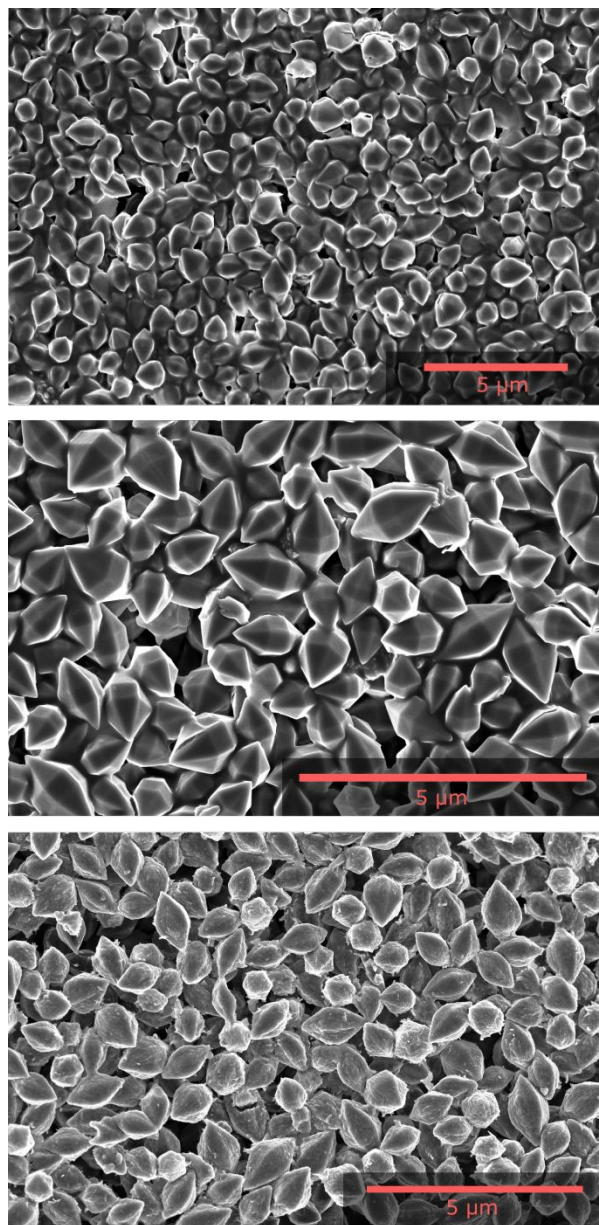


Figure S19. SEM micrographs of iron(III) fumarate microparticles solvothermally synthesized in DMF (**top**), stored for 6 months in ethanol (**middle**) and stored for 2 weeks in water (**bottom**).

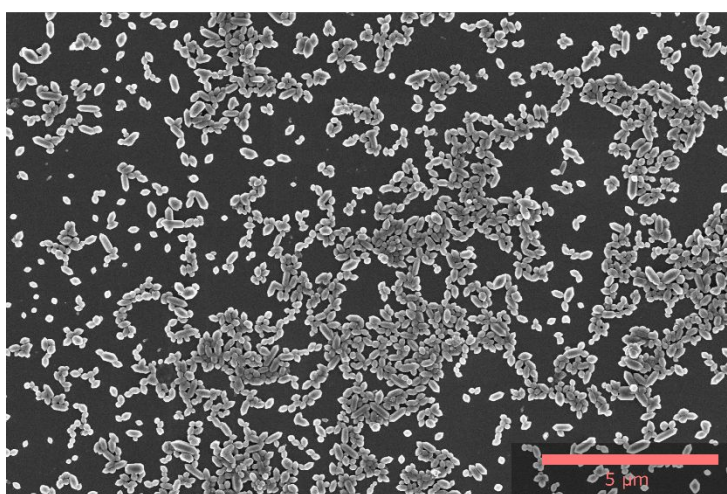
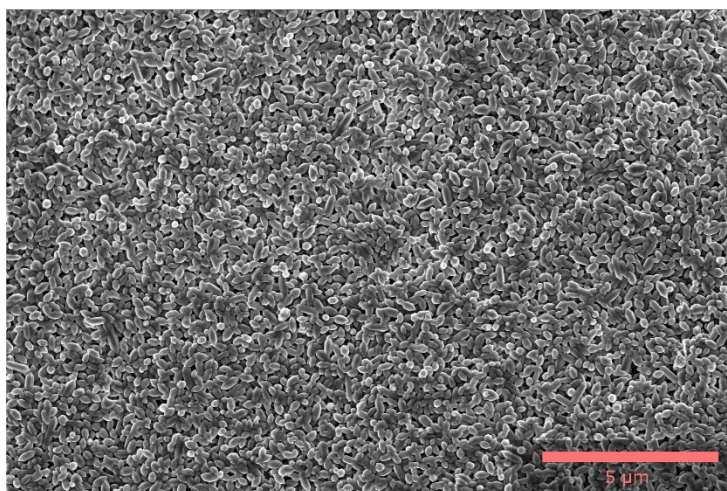
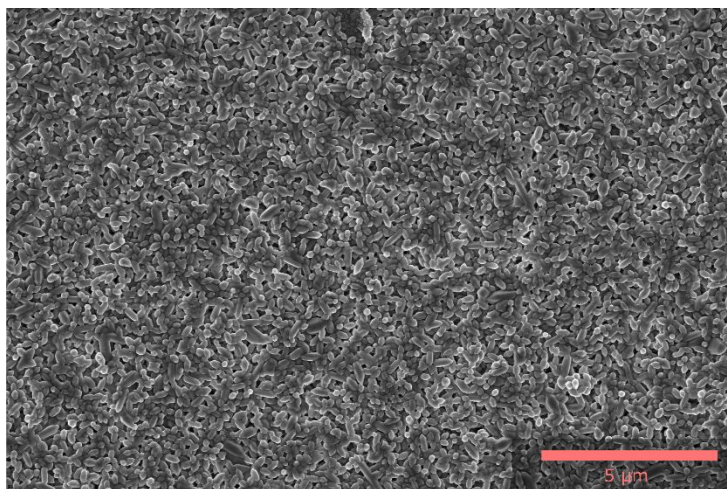


Figure S20. Dipyramidal iron(III) fumarate nanoparticles microwave-synthesized in DMF (**top**), stored for 3 months in ethanol (**middle**) and stored for 1 day in water (**bottom**).

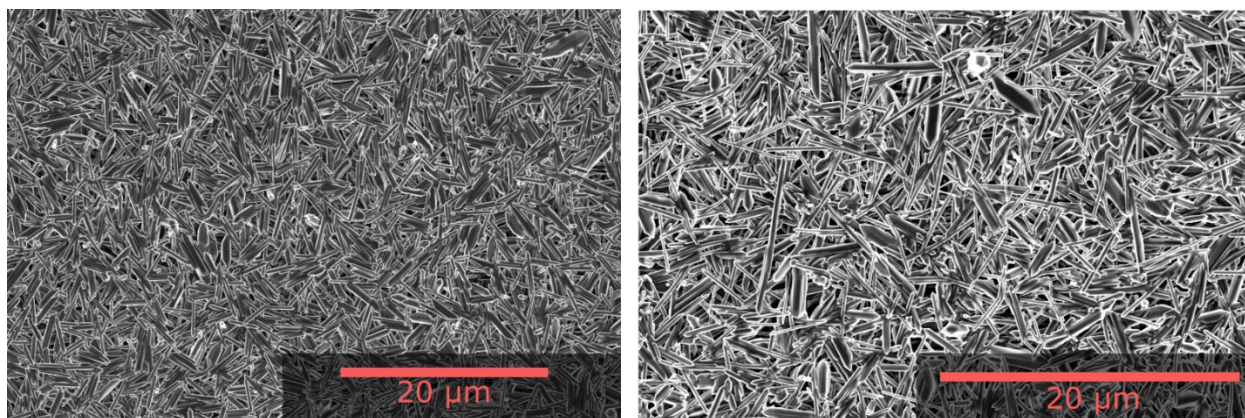


Figure S21. SEM micrographs of needle-shaped iron(III) fumarate microparticles freshly prepared from water (**left**) and stored for 2 months in ethanol (**right**).

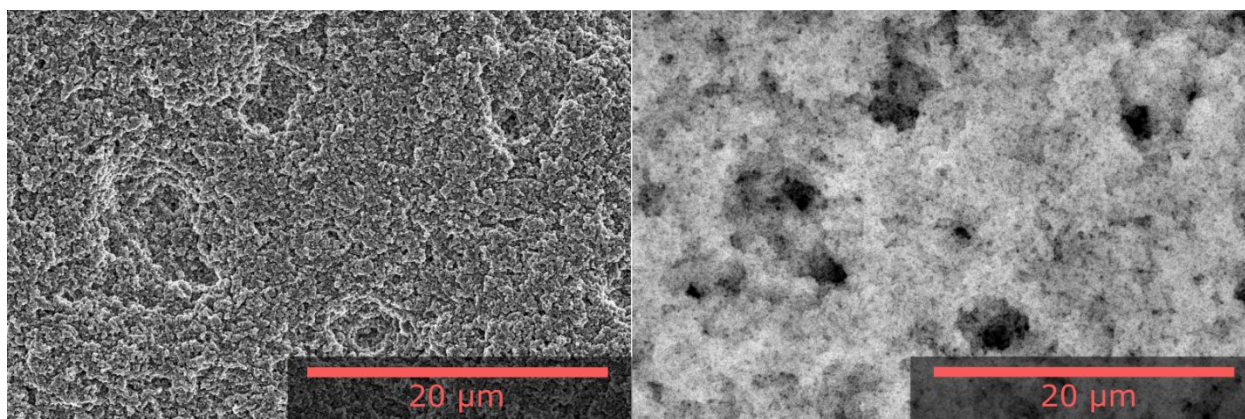


Figure S22. SEM micrographs of spherical iron(III) fumarate nanoparticles that were stored for 6 months in ethanol. On the left and right side the same spot in each sample is depicted. The micrographs on the left side were recorded at 3 kV using a secondary electron detector, the micrographs on the right side were recorded at 15 kV using a mirror detector. No formation of needle morphology can be seen in this picture showing the stability of the spherical phase.

Dynamic Light scattering experiments

To evaluate the colloidal stability and size of the particles in various solvents, dynamic light scattering (DLS) measurements were performed. Generally, DLS measurements result in a hydrodynamic particle diameter. This diameter is corresponding to a hypothetical sphere that is exhibiting the same solvent-mobility as the respective sample particles. The hydrodynamic diameter does not give information on particle morphology and is difficult to interpret in case of non-spherical particles. Additionally, DLS measurements require the particles to move freely. In case of large particles ($\sim 1 \mu\text{m}$) the measurements become less reliable. For these reasons, the DLS data that is presented here is most accurate for the nano-sized iron(III) fumarate variants.

The number based particle size distributions of all iron(III) fumarate types in different solvents are shown in Figure S23. Generally, the particles show excellent colloidal stability when dispersed in ethanol and Milli-Q water. In HBG buffer (pH 7.4, 10 mM) the dipyramidal iron(III) fumarate nanoparticles retain their colloidal stability, while the spherical nanoparticles exhibit slight signs of agglomeration. The measurements in HEPES buffer (pH 7.4, 10 mM) again show slight agglomeration of the spherical nanoparticles as well as a shifted particle size towards a larger hydrodynamic diameter. The dipyramidal nanoparticles additionally show a broadened size distribution in HEPES buffer.

The mean and standard deviation of the main fractions of the respective particles is shown in Table S3. The particle sizes in these solvents are generally in agreement with each other but show slight deviations in HEPES buffer. This can be further confirmed in the following zeta-potential measurements.

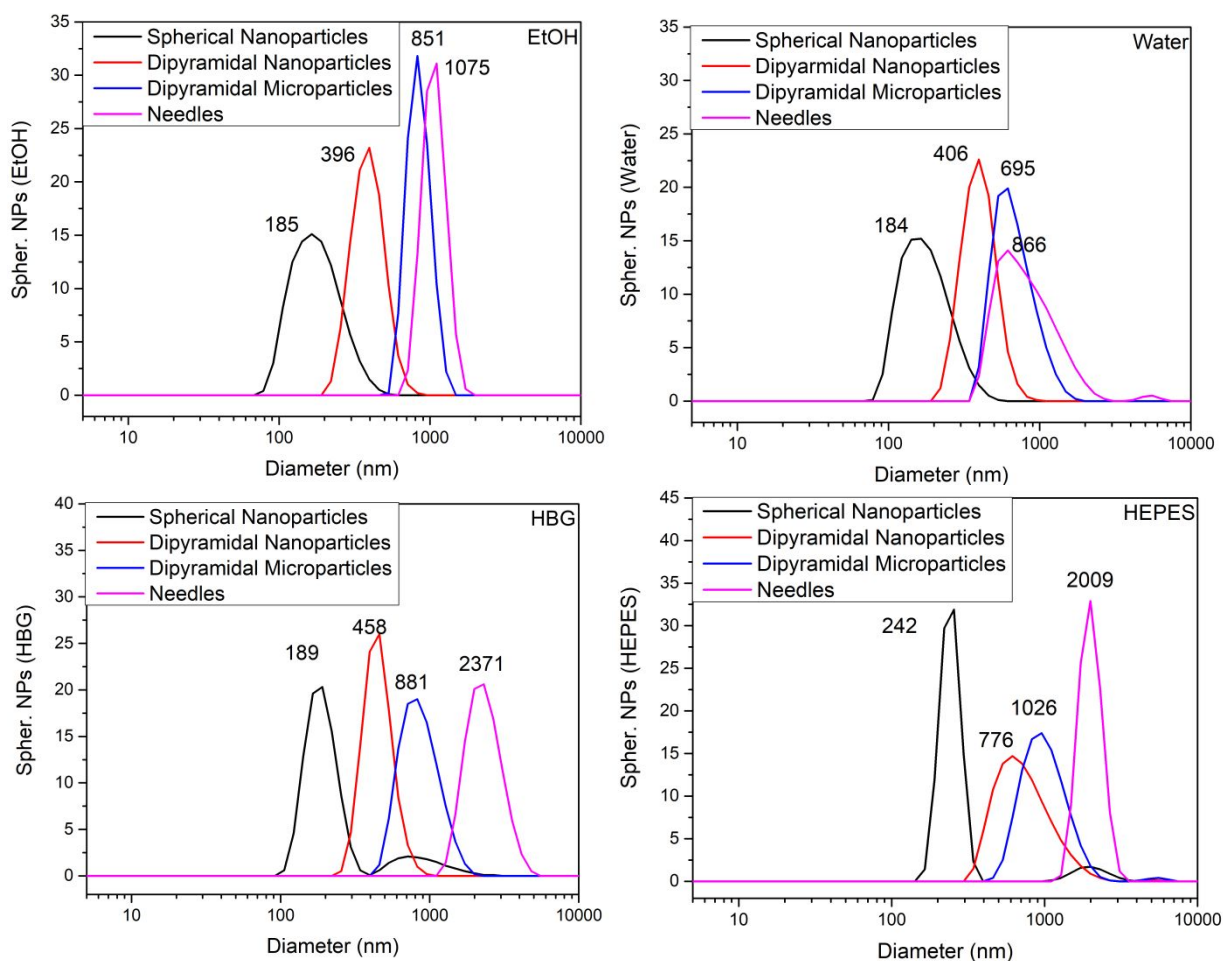


Figure S23. Number based particle size distributions of the different iron(III) fumarate variants in different solvents (**top-left:** ethanol, **top-right:** water, **bottom-left:** HBG (pH = 7.4), **bottom right:** HEPES (pH = 7.4)).

Table S3. Mean size of the dominant fractions of the respective iron(III) fumarate types in different media as well as the corresponding standard deviation σ .

Solvent	Spherical Nanoparticles		Dipyrarmidal Nanoparticles		Dipyrarmidal Microparticles		Needles	
	Diameter (nm)	σ (nm)	Diameter (nm)	σ (nm)	Diameter (nm)	σ (nm)	Diameter (nm)	σ (nm)
Ethanol	185	70	396	97	851	150	1075	188
Water	184	70	406	100	695	221	866	327
HBG (pH = 7.4)	189	45	458	106	881	264	2371	653
HEPES (pH = 7.4)	242	37	776	344	1026	337	2009	344

In addition to particle size, zeta potential measurements were performed to assess the colloidal stability and surface charge of the different iron(III) fumarate types. For these experiments, aqueous dispersions of the respective particles (0.1 mg/mL) were titrated from pH = 2 – 8.5 with a step size of $\Delta\text{pH} = 0.5$. At each step, the zeta potential of the particles was determined in three measurements. Figure S24 shows the mean values of these experiments along with their standard deviation. In water, all particles are positively charged with a zeta-potential ranging between 27 mV in case of the spherical nanoparticles to 47 mV for the crystalline needles. As expected, the zeta-potential of the particles becomes increasingly smaller with increasing pH ending between 1 mV and 3 mV at $\sim\text{pH} = 8.5$. There are subtle differences in the behavior of the particles: The zeta-potential of the smallest nanoparticles features initially the lowest values. However, there is no clear size dependency in the initial values of the three larger iron(III) fumarate variants. The Zeta-potential of the nanoparticles types features a plateau between pH = 5-8 which might be attributed to a reaction on the particles large surface, possibly by the deprotonation of uncoordinated linker molecules. Naturally, the larger microparticle variants are less affected by this.

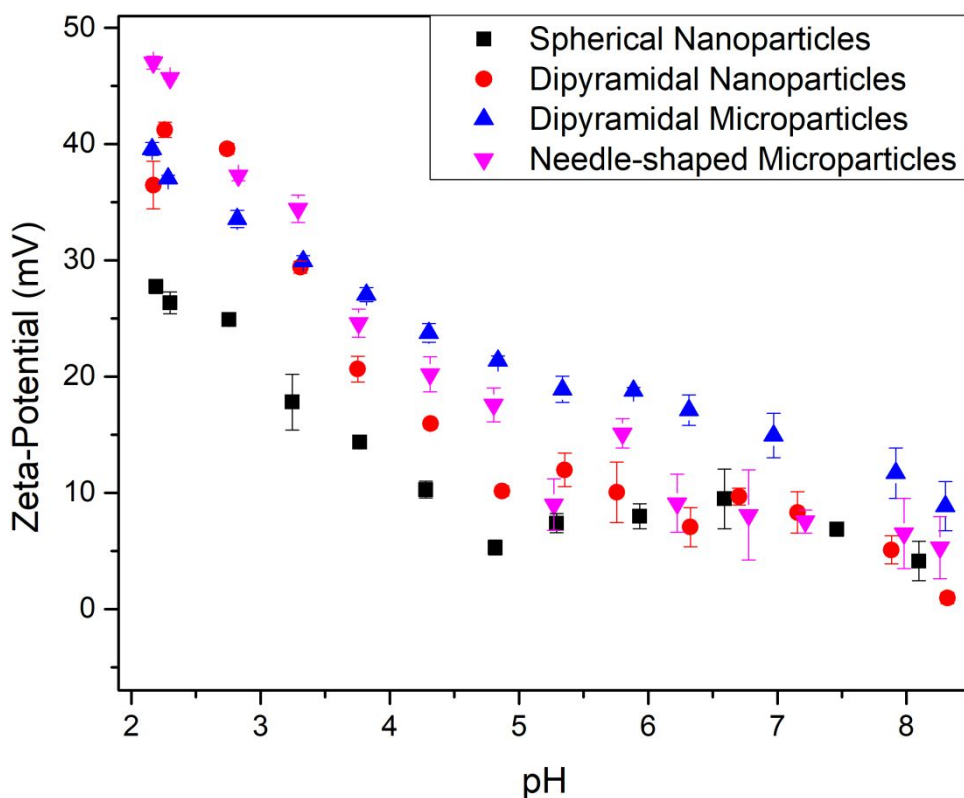


Figure S24. pH dependent zeta-potential of all iron(III) fumarate particles in water.

In addition to these measurements in aqueous solution, the zeta-potential of iron(III) fumarate in buffers (HBG pH 7.4 10 mM, and HEPES pH 7.4 10 mM) that are relevant to this system has been determined. This data is in agreement with the DLS measurements. In HEPES buffer, the particles feature a zeta-potential below $|5|$ mV, which is in agreement with their increased agglomeration. In HBG buffer on the other hand, the charge on the particle surface was inverted with potentials ranging from -10 mV for the spherical nanoparticles to -22 mV for the needle-shaped morphology. These values also confirm the stabilizing effect in comparison to HEPES buffer that could be seen in DLS measurements.

Table S4. Zeta-potential data of iron(III) fumarate particles in HBG and HEPES buffer at pH = 7.4.

Solvent	Spherical Nanoparticles		Dipyramidal Nanoparticles		Dipyramidal Microparticles		Needles	
	Zeta Potential (mV)	σ (mV)	Zeta Potential (mV)	σ (mV)	Zeta Potential (mV)	σ (mV)	Zeta Potential (mV)	σ (mV)
HBG (7.4)	-10	4	-14	4	-17	3	-22	4
HEPES (7.4)	5	5	-5	6	-3	3	4	1

Table S5. Analysis data on the thermogravimetric degradation of the iron(III) fumarate variants.

	Spherical Nanoparticles	Needle-shaped Microparticles	Dipyramidal Microparticles	Dipyramidal Nanoparticles
Residual mass dried framework	93.7%	97.2%	92.0%	94.8%
Onset of framework degradation	267.4 °C	273.5 °C	259.2 °C	285.0 °C
Residual mass	38.5%	40.2%	40.7%	37.2%

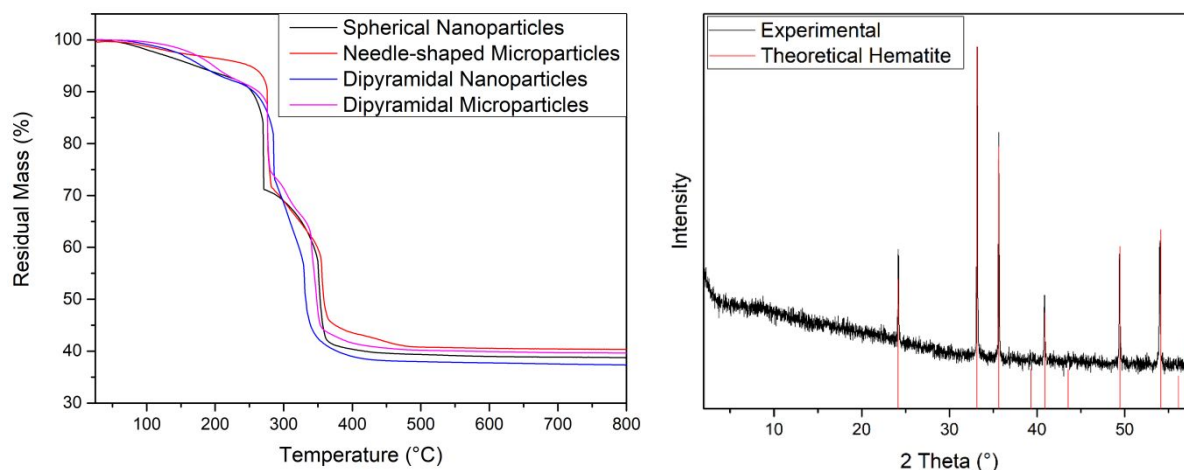


Figure S25. Left: Degradation curves of the different iron(III) fumarate variants. **Right:** X-ray diffraction pattern of the resulting degradation product.

Table S6. The lattice parameters of the X-ray amorphous spherical iron(III) fumarate nanoparticles were determined with electron diffraction on the basis on the theoretical fully dry-pore ($a = 9.78$, $c = 14.83$) and fully open-pore ($a = 13.87$, $c = 12.66$) MIL-88A crystal structures published by Serre.¹ For the spherical nanoparticle sample, our experimentally observed d-values are between these two extreme cases but closer to the open pore structure.

Laue indices	011	020	$\bar{1}32$	$\bar{1}35$	$\bar{2}57$
Theoretical lattice distances of closed-pore MIL-88A[Å] ¹	7.35	4.2	2.93	2.17	1.43
Theoretical lattice distances of open-pore MIL-88A[Å] ¹	8.72	6.01	3.69	2.21	1.51
Experimental lattice distances [Å]	7.8	4.1	2.92	2.17	1.47

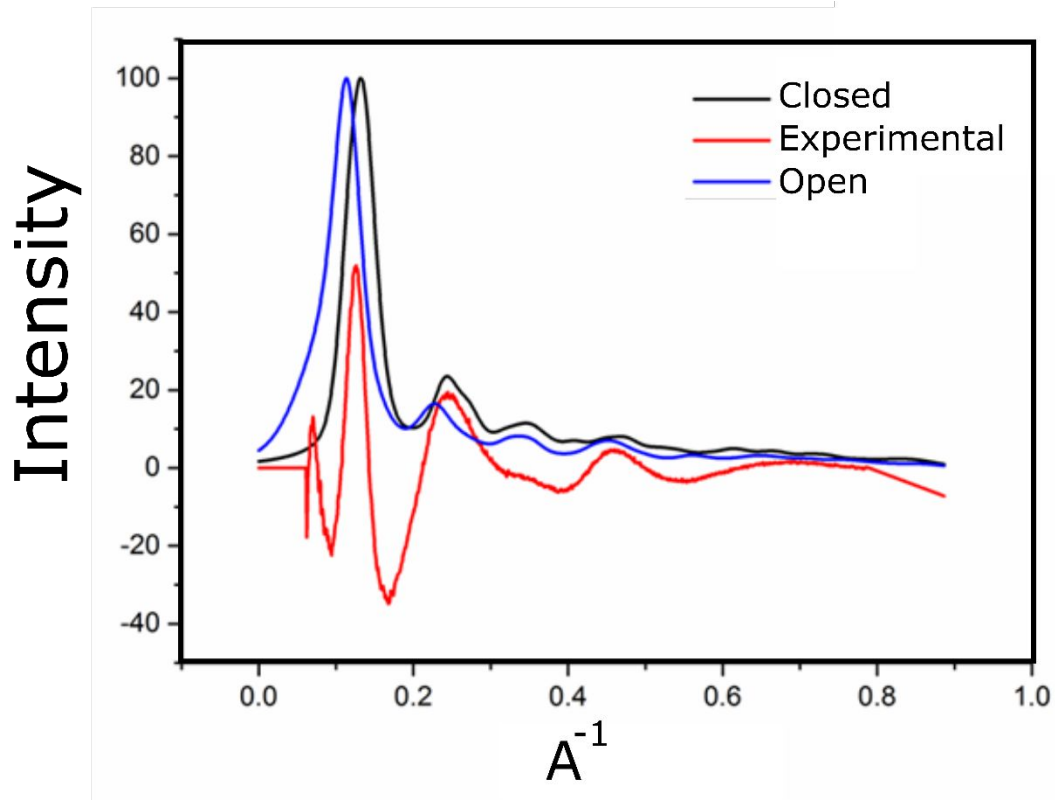


Figure S26. Simulated electron diffraction patterns of closed pore and open pore MIL-88A compared experimental azimuthally integrated and background subtracted electron diffraction pattern of X-ray amorphous iron(III) fumarate nanoparticles.

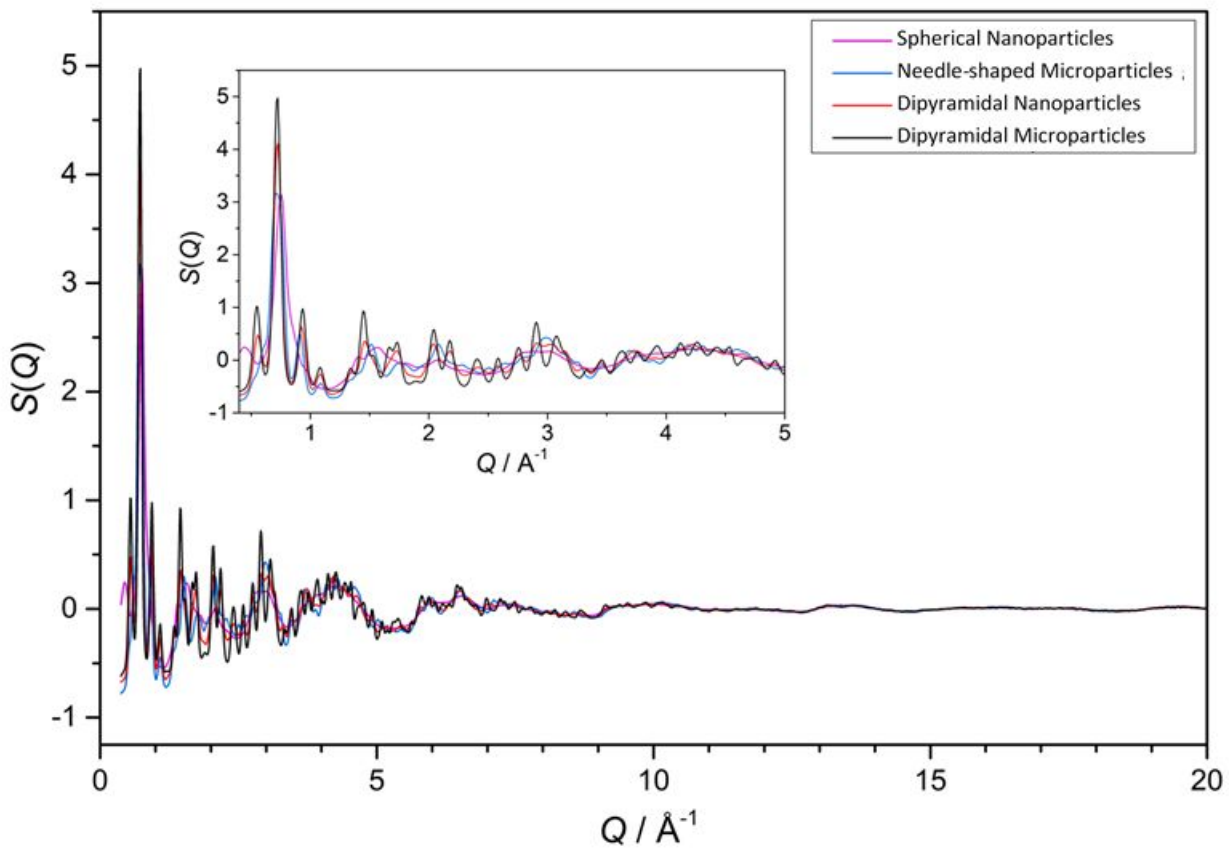


Figure S27. X-ray structure factors $S(Q)$ s of the four samples.

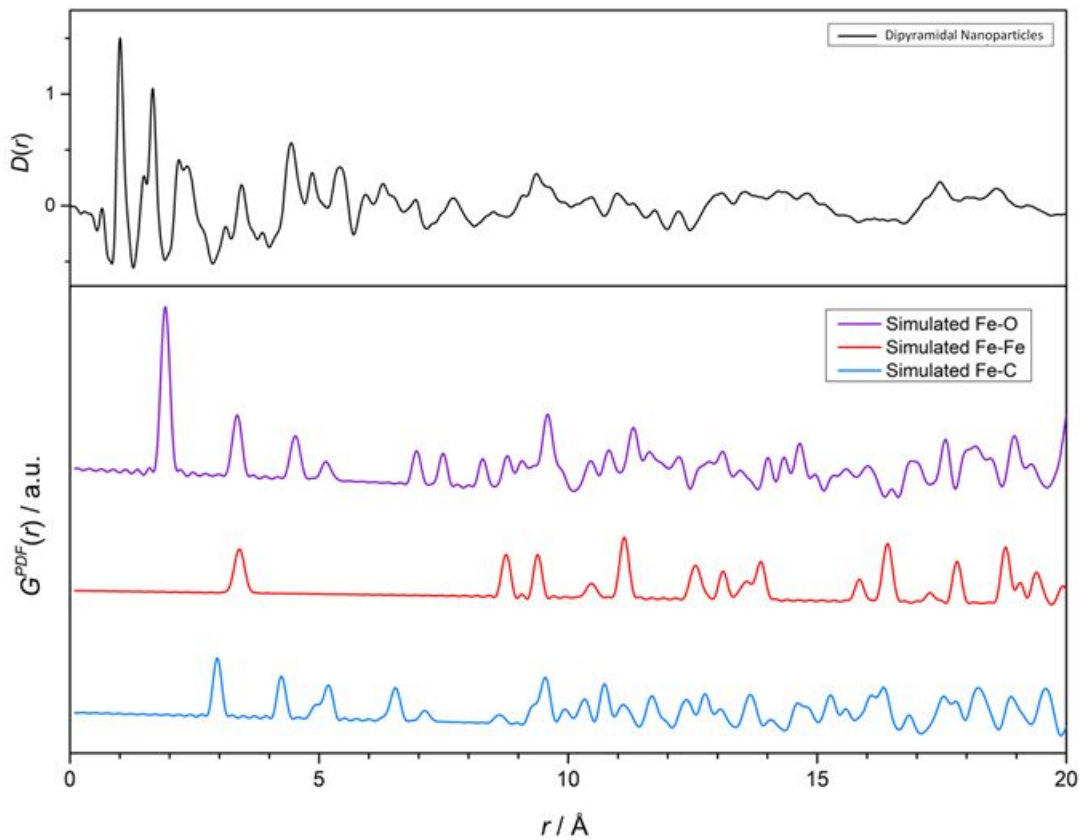


Figure S28. $D(r)$ of MIL-88A Dipyrromidal nanoparticles (upper) and simulated partial PDFs of Fe-O (purple), Fe-Fe (red), and Fe-C (blue) atom-atom correlations using PDFGUI and the corresponding MIL-88A Open CIF file¹ (lower).

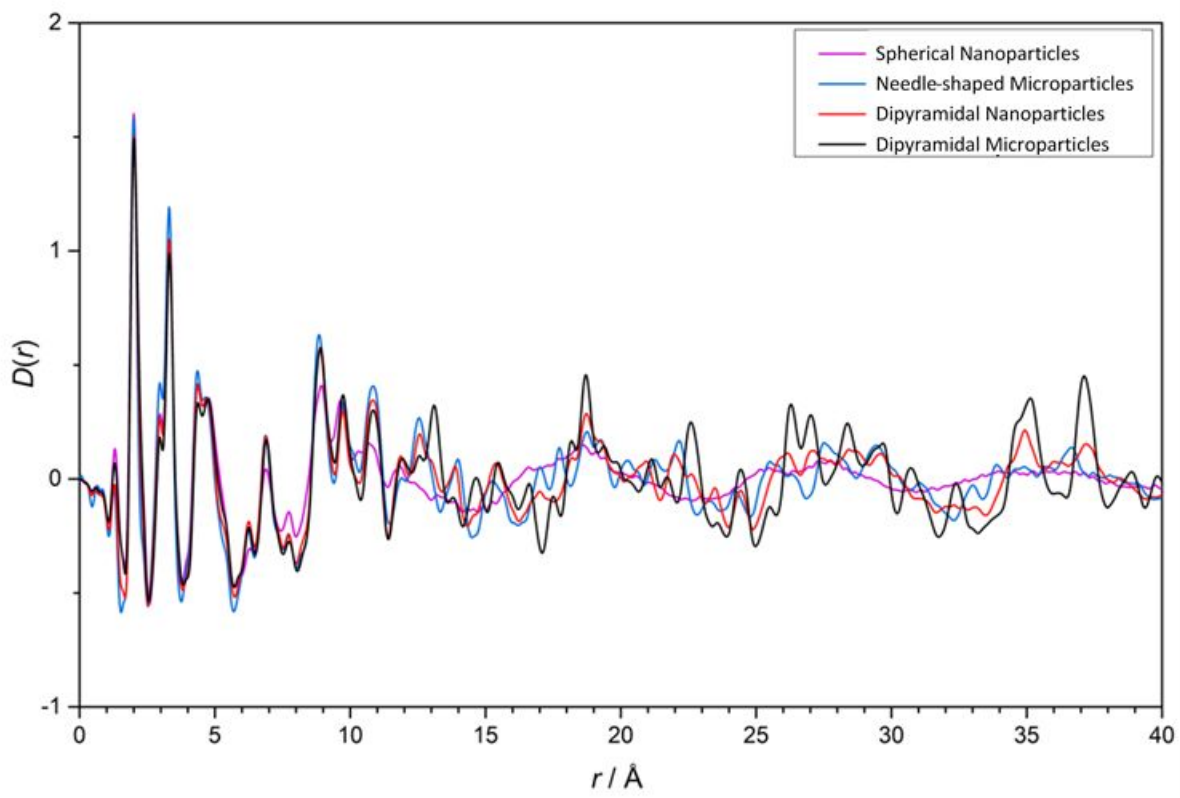


Figure S29. Pair distribution functions $D(r)$ of the four samples.

Table S7. BET-analysis data of iron(III)-fumarate.

Sample	BET surface area	Relative pressure range	c	Correlation coefficient
Spherical Nanoparticles	446 m ² /g	0.05-0.17	154	0.999
Dipyramidal Nanoparticles	264 m ² /g	0.15-0.27	43	0.999
Dipyramidal Microparticles	212 m ² /g	0.04-0.15	428	0.999
Needle-shaped Microparticles	119 m ² /g	0.002-0.02	1131	0.999

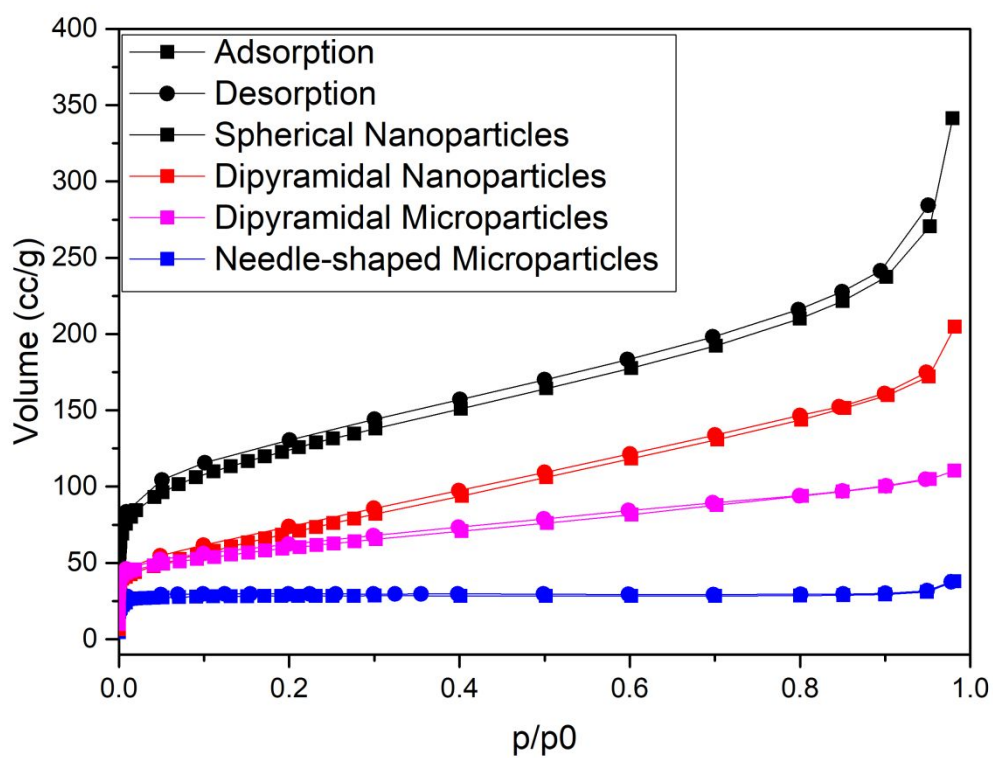


Figure S30. Nitrogen sorption isotherms of the four iron(III) fumarate types (left)

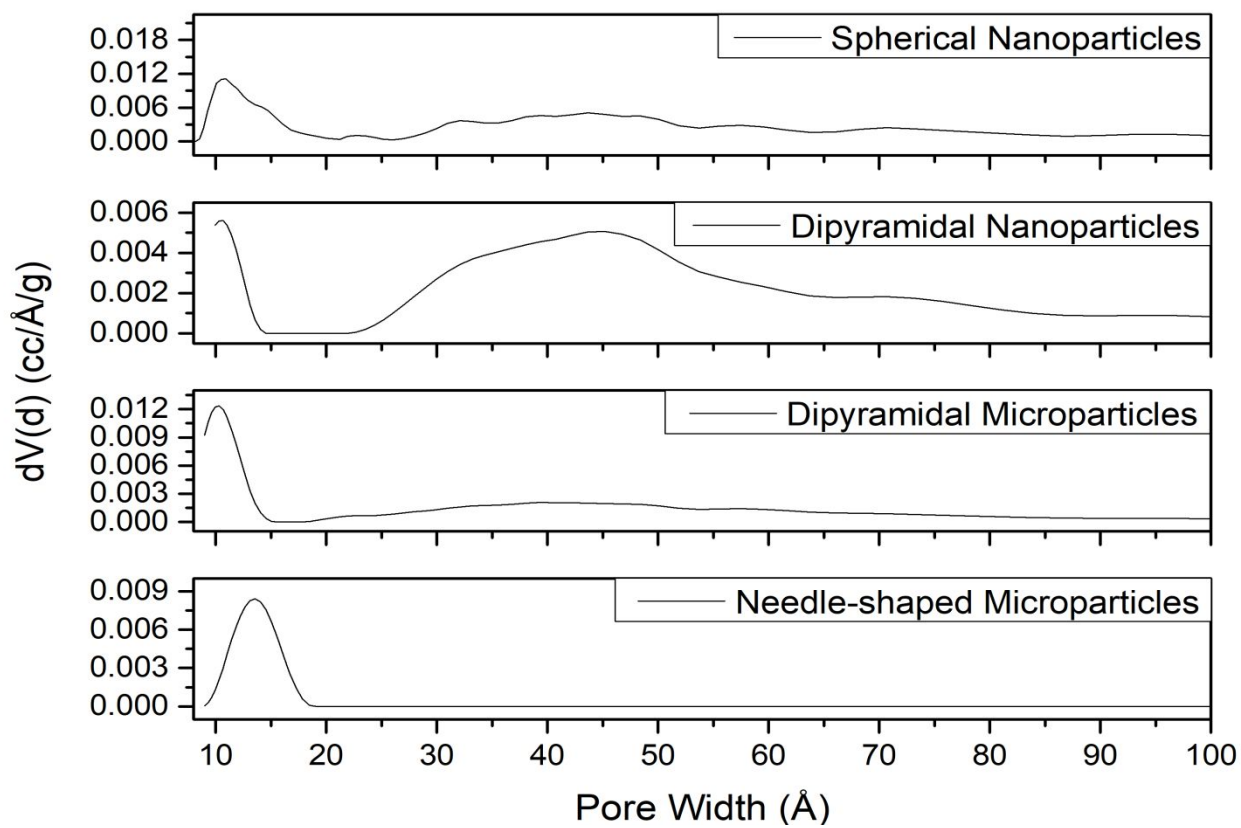


Figure S31. Pore size distribution of the 4 iron(III) fumarate variants as determined with nitrogen sorption.

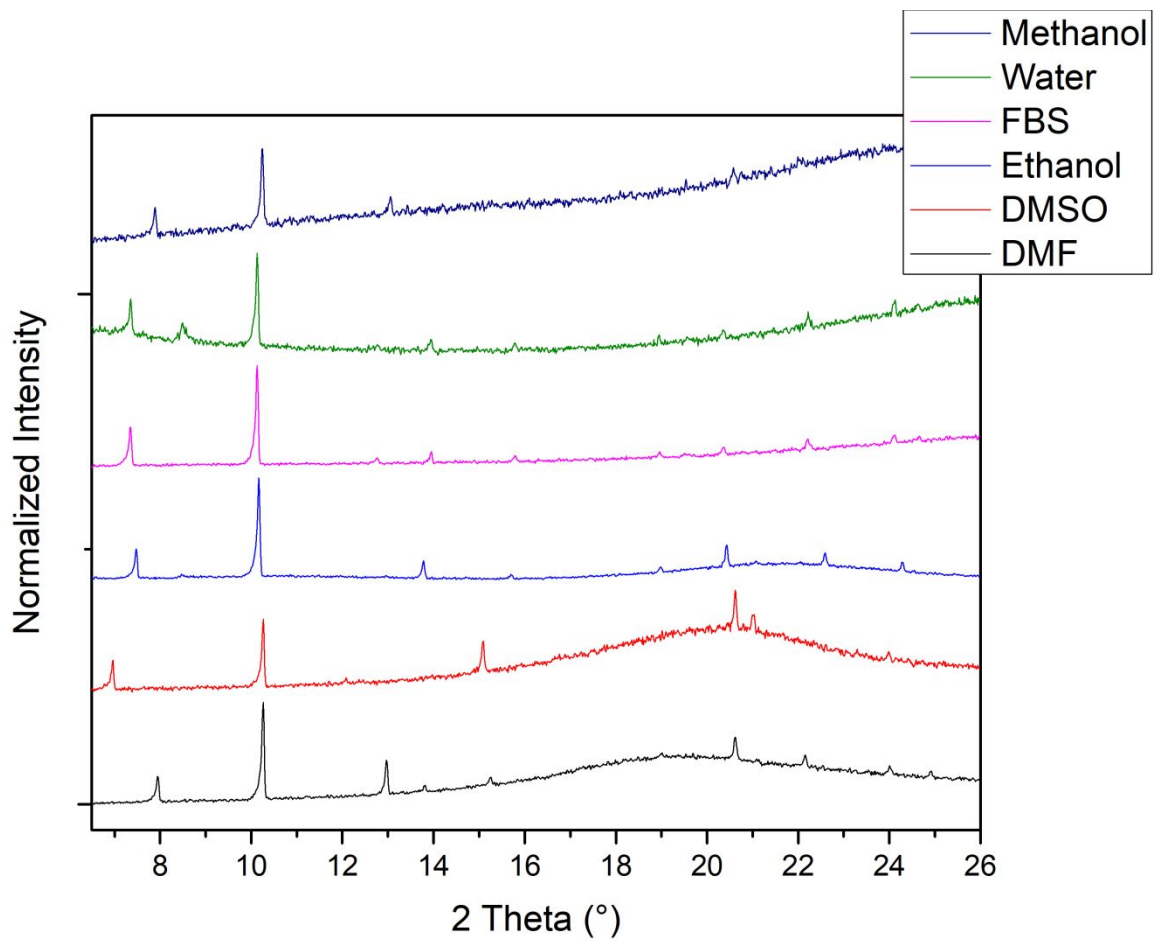


Figure S32. *In-situ* X-ray diffraction patterns of dipyrroimid iron(III) fumarate microparticles.

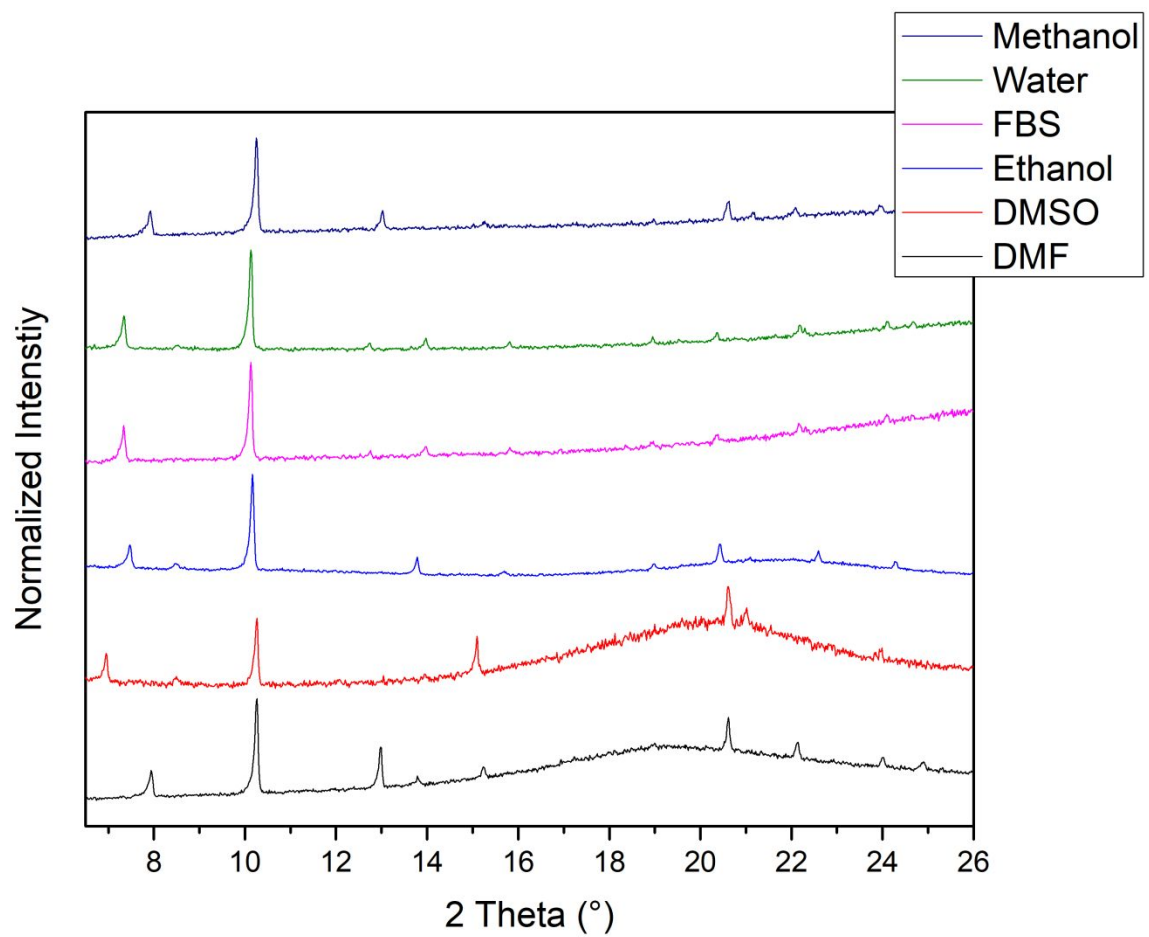


Figure S33. In-situ X-ray diffraction patterns of dipyramidal iron(III) fumarate nanoparticles.

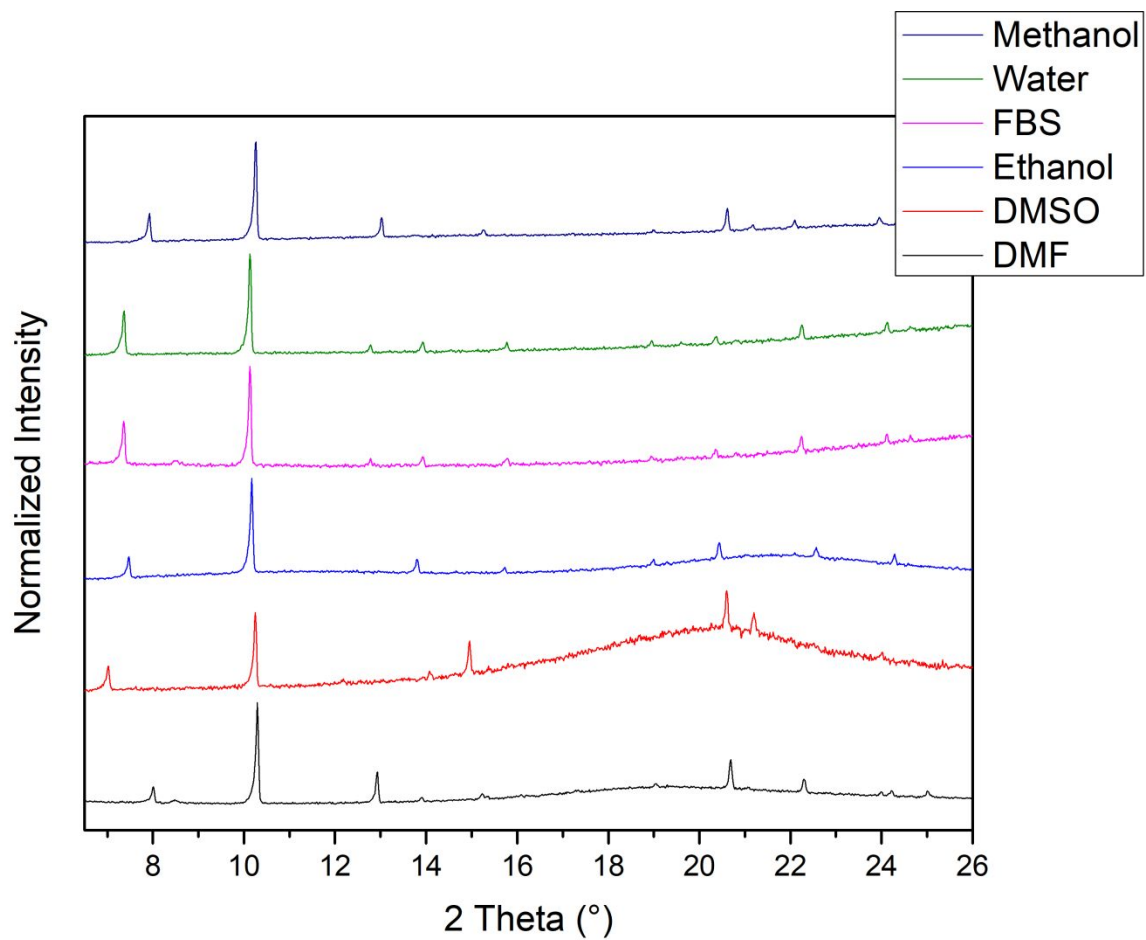


Figure S34. In-situ X-ray diffraction patterns of needle-shaped iron(III) fumarate microparticles.

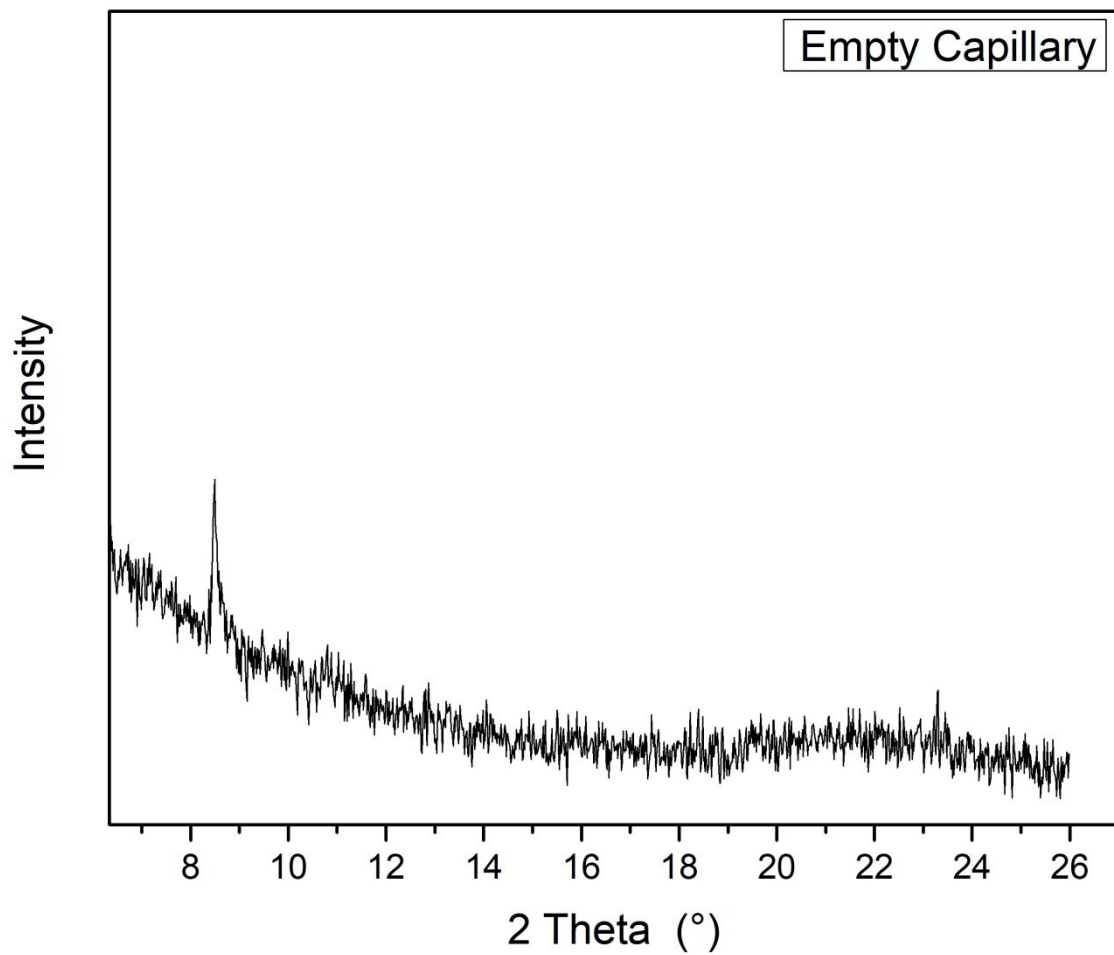


Figure S35. X-ray diffraction data of an empty glass used during *in-situ* X-ray diffraction experiments

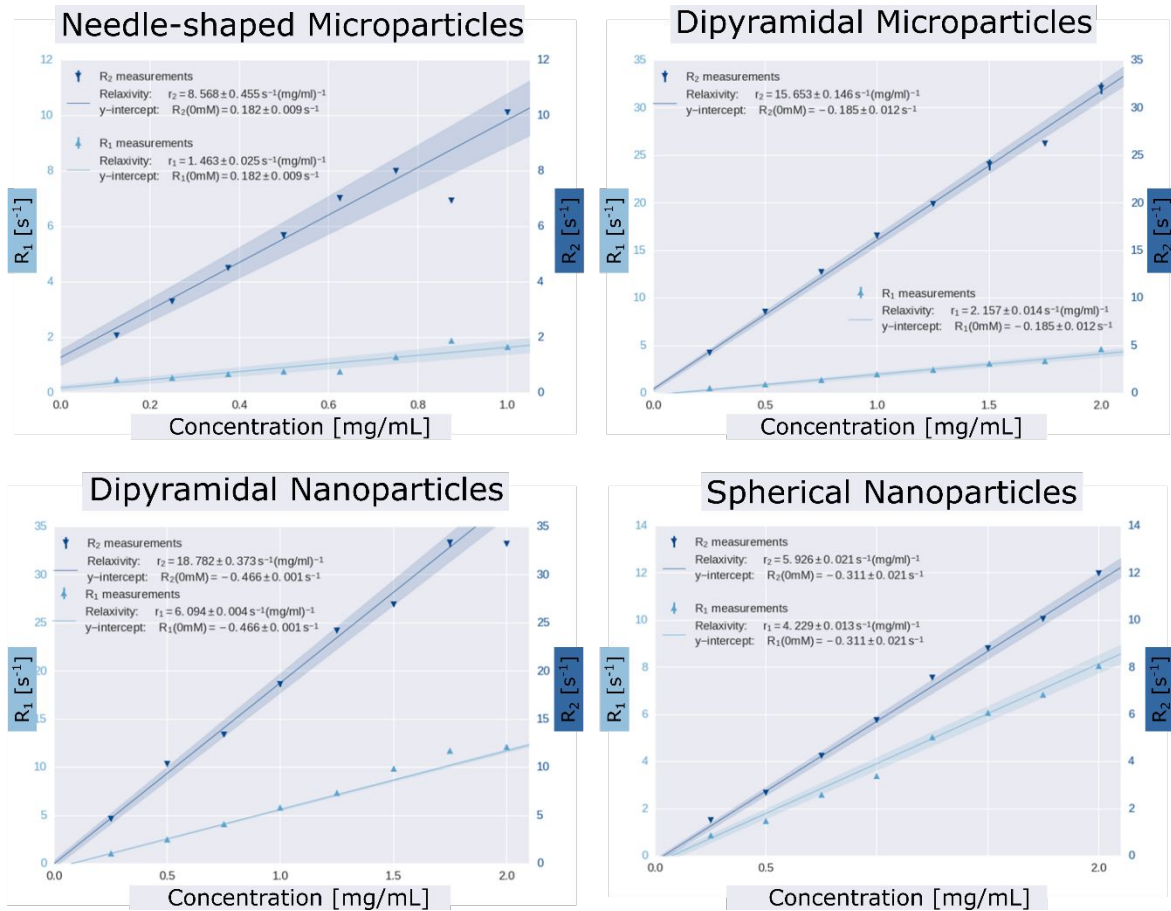


Figure S36. Determination of the mass-based relaxivities in accordance to Table 4 for the respective iron(III) fumarate variants. Experimentally determined inverse relaxation times are plotted vs iron(III) fumarate concentration. Relaxivity values can be determined from the slope of the linear plot.

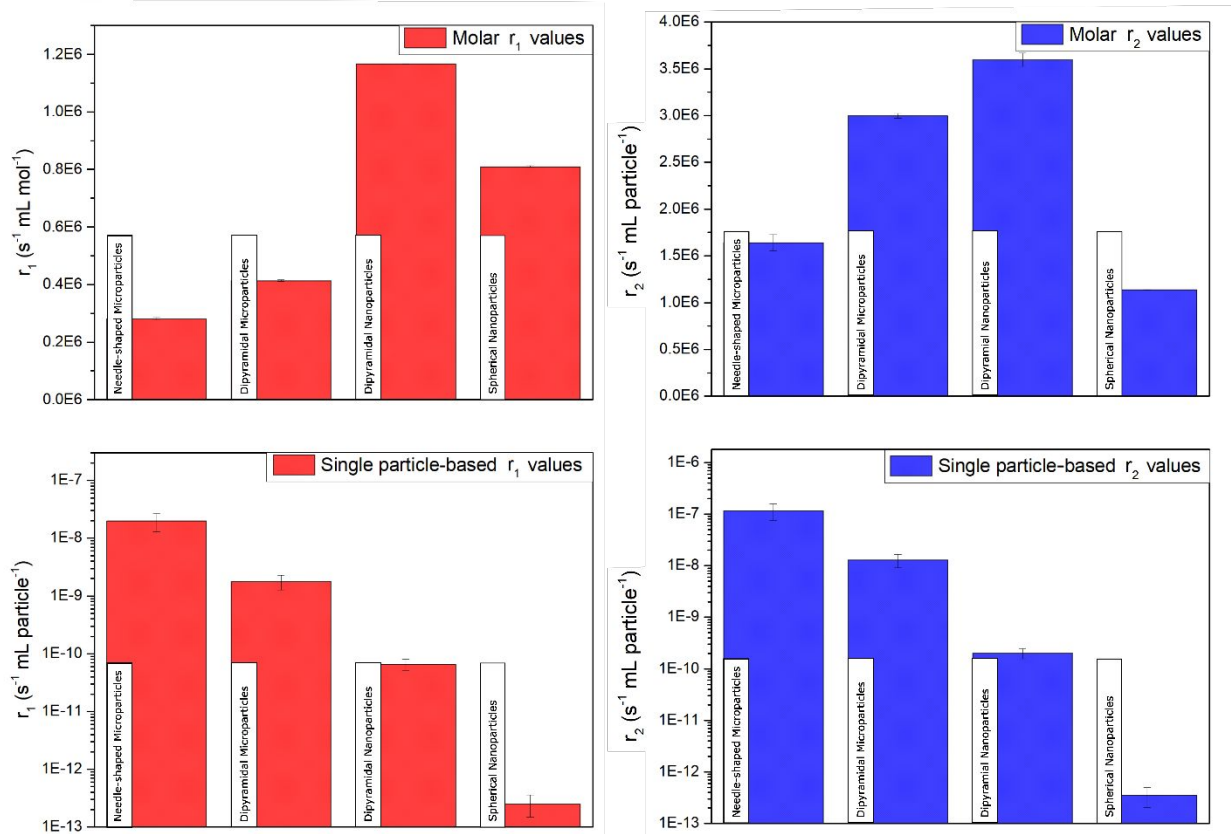


Figure S37. MRI relaxivities of the four iron(III) fumarate particles with different focus. The data that is presented as mass-based relaxivities in Table 4 and Figure S36 can be converted to other relaxivity values for better comparison. For evaluating the relaxivities per single particle we were approximating the particle size of the respective iron(III) fumarate variants from SEM measurements. In our estimate, we treated the dipyrarnidal microparticles (diameter 1200 ± 200 nm) and the spherical nanoparticles (diameter 50 ± 12 nm) as spheres calculating their volume from their particle size distribution (Figure S25). The morphology of the needle-shaped microparticles was approximated as a cylindrical shape and their particle volume calculated from their mean diameter (975 ± 420 nm) and length (10 ± 2 μ m). The volume of the dipyrarnidal nanoparticles (length 400 ± 95 nm, diameter 185 ± 30 nm) was approximated as a cylinder with 2 cone shaped tips, featuring a ratio of 1/3 : 1/3 : 1/3. With these approximations and assuming an open porous MIL-88A structure with a crystallographic density of 0.902 g/cm³,² the mass based relaxivities were transformed to single particle-based relaxivities. Similarly, these values can be transformed into relaxivities that are normalized towards single iron(III)-ions in the structure assuming a 29.2 wt% iron in the crystal structure¹. For better comparison with commercially available MRI contrast coordination complexes these values were additionally normalized towards the molar quantity of iron(III) ions.

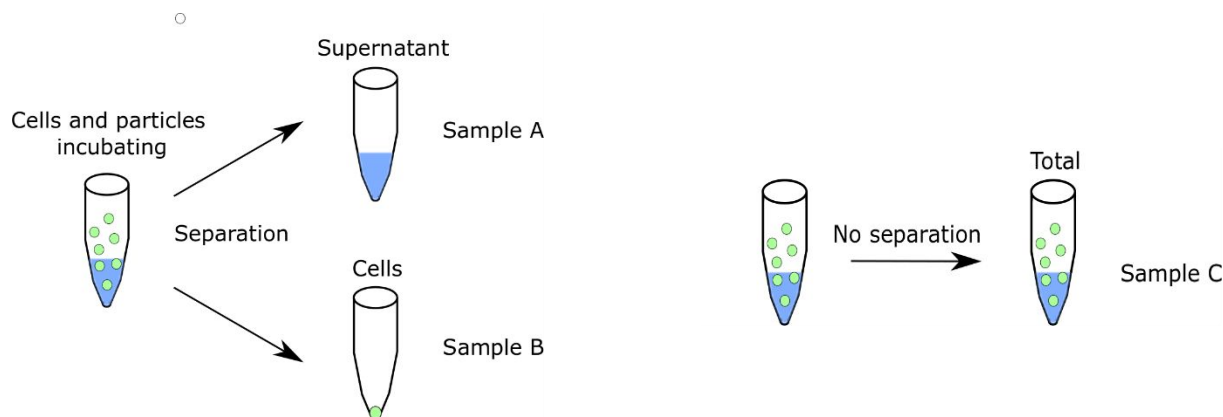


Figure S38. To measure the cell association of the respective iron(III) fumarate variants ICP-OES measurements were performed. For sample preparation HeLa-Cells (500 μL) were incubated for 24 h at 37 $^{\circ}\text{C}$ with aqueous solutions of iron(III) fumarate particles (100 $\mu\text{g}/\text{mL}$) in a 24 well plate. After this incubation period cells and supernatant were separated. The cells were washed twice with phosphate buffered saline (500 μL), these washing solutions were then unified with the incubation-supernatant (**Samples A**). The cells were recovered separately by adding 500 mL of aqueous triton solution (1%) with an additional washing step afterwards (500 μL H_2O) **Samples B**). To quantify the iron content in the extracellular medium and associated with cells (100%), control samples in which incubation solution and cells were not separated were additionally prepared (**Samples C**). As a background control of physiological iron content, cells were treated in the same fashion without addition of iron(III) fumarate particles (**Cells A-C**). This incubation was additionally repeated with using an iron(III) chloride solution (29.2 $\mu\text{g}/\text{mL}$) (**FeCl₃ A-C**). All samples labelled with A and B were prepared in triplets. Prior to the measurements the samples were dried in an oven (100 $^{\circ}\text{C}$, 48 h). The residuals were dissolved in HNO_3 (10%) and the respective iron content of the solutions analyzed with ICP-OES. The measured iron contents can be found in

Table S8.

Table S8. Iron Content in cell association experiments determined from ICP-OES measurements.

Sample	Iron content ($\mu\text{g/mL}$)
Spherical Nanoparticles A	22.63 ± 0.25
Dipyramidal Microparticles A	10.49 ± 0.24
Needle-shaped Microparticles A	8.61 ± 0.33
Dipyramidal Nanoparticles A	20.44 ± 0.49
FeCl_3 A	31.66 ± 0.08
Spherical Nanoparticles B	4.28 ± 0.18
Dipyramidal Microparticles B	18.00 ± 0.55
Needle-shaped Microparticles B	20.12 ± 0.41
Dipyramidal Nanoparticles B	8.71 ± 0.20
FeCl_3 B	0.82 ± 0.14
Cells A	Below threshold
Cells B	Below threshold
Spherical Nanoparticles C	28.60
Dipyramidal Microparticles C	30.42
Needle-shaped Microparticles C	30.54
Dipyramidal Nanoparticles C	30.30
FeCl_3 C	31.69
Cells C	1.06

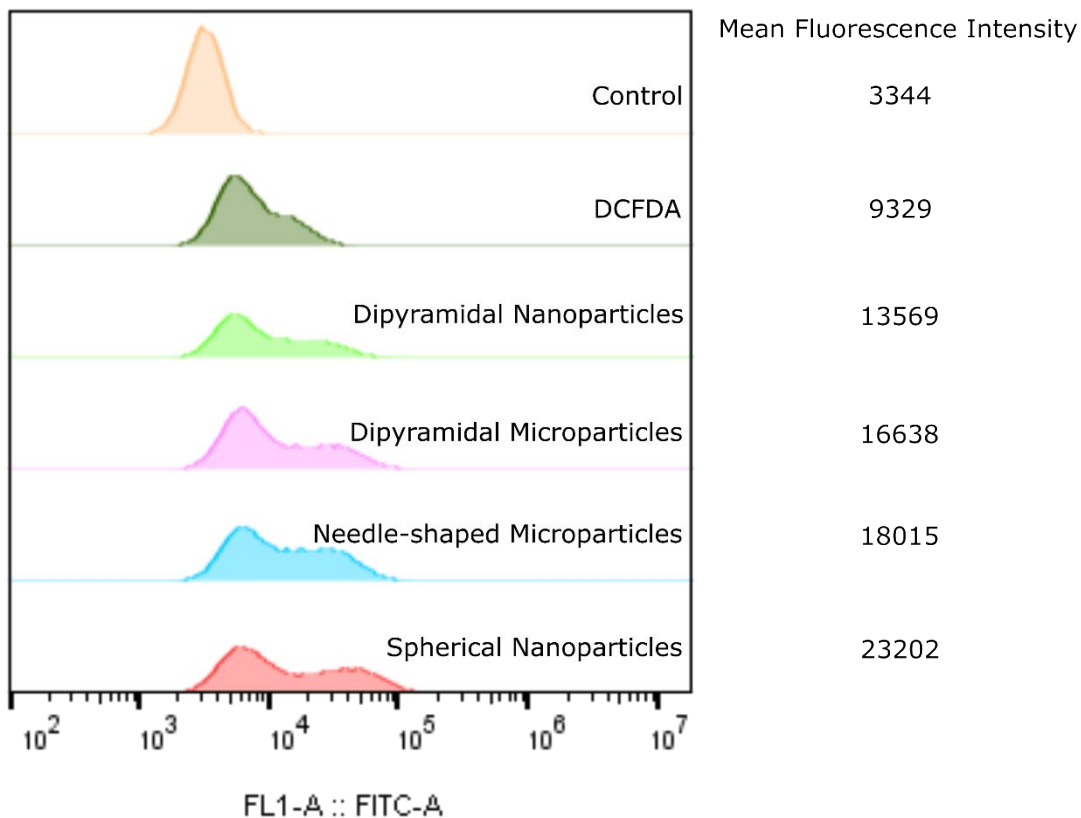


Figure S39. Investigation of reactive oxygen species (ROS) generation. 60.000 cells were seeded per well on a 24 well plate. Two wells were treated under the same conditions and pooled for final evaluation by flow cytometry. Cells were treated for 3 h with 20 μ M DCFDA alone or together with the four different iron(III) fumarate particles at a concentration of 100 μ g/mL. Afterwards the medium was removed, cells were washed with PBS, trypsinized, and analyzed using a CytoFLEX S flow cytometer (Beckman Coulter, U.S.). 4',6 diamidino 2 phenylindole (DAPI) was added at 2 μ g/mL prior to the measurement to discriminate viable and dead cells. The cellular fluorescence was assayed by excitation of DAPI at 405 nm and detection of emission at 450 nm, the excitation of DCFDA at 488 nm and detection of emission at 520 nm. Flow cytometry data were analyzed using FlowJo 7.6.5 (FlowJo, LLC, Ashland, OR).

4. Calculations on the Theoretical Particle Surface Area

Equation 1: Surface of a single sphere $S = 4 \pi r^2$

Equation 2: Volume of a single sphere $V = \frac{4}{3} \pi r^3$

The change in BET surface area of the iron(III) fumarate microparticles variants (Table S7) cannot only be explained with just the varying particle sizes. Using the equations above and approximating a spherical morphology for the dipyramidal microparticle iron(III) fumarate variant, the outer surface area of a single such particle with a diameter of 1600 nm can be calculated at $8.4 \times 10^{-8} \text{ cm}^2$. The corresponding particle volume is at $2.4 \times 10^{-12} \text{ cm}^3$. Assuming a density of 1.55138 g/cm^3 (crystallographic density of dry MIL-88A¹) this results in an outer surface area of $2.4 \text{ m}^2/\text{g}$ for the entire sample. The same calculations result in outer surface area of $13 \text{ m}^2/\text{g}$ for when approximating the dipyramidal nanoparticle iron(III) fumarate variant. The respective increase of surface area in these samples however exceeds this approximation. As all samples exhibit the same crystal structure this effect either stems from pore clogging and texturing. We assume that both of these effects are present. On the one hand the pore size distributions of the dipyramidal microparticles and dipyramidal nanoparticles exhibit mesopores. On the other hand thermogravimetric analysis shows a ~ 3 fold increase of residual solvent molecules in the pores that was not removable even under heating in high-vacuum.

When comparing spherical iron(III) fumarate to the other iron(III) fumarate microparticles crystallinity might play an effect as well: Using the equations above, a single spherical particle with a diameter of 60 nm exhibits a volume of $1.13 \times 10^{-16} \text{ cm}^3$ and an outer surface area of $1.13 \times 10^{-10} \text{ cm}^2$. Assuming crystallinity and a density of 1.55138 g/cm^3 (crystallographic density of dry MIL-88A¹) this results in a theoretical surface area of $64 \text{ m}^2/\text{g}$. If the same calculations are done for a spherical particle (as this is roughly the shape of the dipyramidal microparticles) with a diameter of 1600 nm the theoretical surface area stemming from the outer surface of the particles can be calculated at $2.4 \text{ m}^2/\text{g}$. The actual increase of the surface area of the spherical nanoparticles to the dipyramidal microparticles is at $244 \text{ m}^2/\text{g}$ and must originate from a different reason. In case of the spherical nanoparticles this can be explained due to texturing during drying or due to effects from their decreased crystallinity.

5. References

1. Serre, C.; Mellot-Draznieks, C.; Surble, S.; Audebrand, N.; Filinchuk, Y.; Ferey, G., Role of solvent-host interactions that lead to very large swelling of hybrid frameworks. *Science* **2007**, 315, (5820), 1828-31.
2. Chalati, T.; Horcajada, P.; Gref, R.; Couvreur, P.; Serre, C., Optimisation of the synthesis of MOF nanoparticles made of flexible porous iron fumarate MIL-88A. *J. Mater. Chem.* **2011**, 21, (7), 2220-2227.
3. Wang, J.; Wan, J.; Ma, Y.; Wang, Y.; Pu, M.; Guan, Z., Metal-organic frameworks MIL-88A with suitable synthesis conditions and optimal dosage for effective catalytic degradation of Orange G through persulfate activation. *RSC Advances* **2016**, 6, (113), 112502-112511.
4. Liu, N.; Huang, W.; Zhang, X.; Tang, L.; Wang, L.; Wang, Y.; Wu, M., Ultrathin graphene oxide encapsulated in uniform MIL-88A(Fe) for enhanced visible light-driven photodegradation of RhB. *Applied Catalysis B: Environmental* **2018**, 221, 119-128.
5. Soper, A. K. *GudrunN and GudrunX: Programs for Correcting Raw Neutron and X-ray Diffraction Data to Differential Scattering Cross Section*; RAL-TR-2011-013; Rutherford Appleton Laboratory Technical Report: Oxfordshire, 2011.
6. Soper, A. K.; Barney, E. R., Extracting the pair distribution function from white-beam X-ray total scattering data. *J. Appl. Crystallogr.* **2011**, 44, (4), 714-726.
7. Mellot-Draznieks, C., Role of computer simulations in structure prediction and structure determination: from molecular compounds to hybrid frameworks. *J. Mater. Chem.* **2007**, 17, (41), 4348.
8. Farrow, C. L.; Juhas, P.; Liu, J. W.; Bryndin, D.; Bozin, E. S.; Bloch, J.; Proffen, T.; Billinge, S. J., PDFfit2 and PDFgui: computer programs for studying nanostructure in crystals. *J Phys Condens Matter* **2007**, 19, (33), 335219.